Subcellular NAD^+ pools are interconnected and buffered by mitochondrial NAD^+

Lena E. Høyland[1*], Magali R. VanLinden[1*], Marc Niere[1*], Øyvind Strømland[1], Suraj Sharma[1,2], Jörn Dietze[3], Ingvill Tolås[1,4], Eva Lucena[1], Ersilia Bifulco[1,5], Lars J. Sverkeli[1,5], Camila Cimadamore-Werthein[1,6], Hanan Ashrafi[1], Kjellfrid F. Haukanes[1], Barbara van der Hoeven[1], Christian Dölle[2,7], Cedric Davidsen[8], Ina K.N. Pettersen[1], Karl J. Tronstad[1], Svein A. Mjøs[9], Faisal Hayat[10], Mikhail V. Makarov[10], Marie E. Migaud[10], Ines Heiland[2,3#], and Mathias Ziegler[1,11#]

1 Department of Biomedicine, University of Bergen, Bergen, 5020, Norway
2 Neuro-SysMed Center, Department of Neurology, Haukeland University Hospital, Bergen, 5021, Norway
3 Department of Arctic and Marine Biology, UiT The Arctic University of Norway, Tromsø, 9037 Norway
4 Current address: Department of Biological Sciences, NTNU Ålesund, Ålesund, 6025, Norway
5 Department of Biological Sciences, University of Bergen, Bergen, 5020, Norway
6 Current address: Medical Research Council Mitochondrial Biology Unit, University of Cambridge, Cambridge Biomedical Campus, Cambridge, CB2 0XY, UK
7 Department of Clinical Medicine, University of Bergen, Bergen, 5020, Norway and K.G. Jebsen Center for Translational Research in Parkinson's Disease, University of Bergen, 5020, Bergen, Norway
8 Department of Heart Disease, Haukeland University Hospital, Bergen, 5021, Norway
9 Department of Chemistry, University of Bergen, Bergen, 5020, Norway
10 Mitchell Cancer Institute, University of South Alabama, Mobile, AL 36604, USA
11 Lead contact, Department of Biomedicine, University of Bergen, Pb 7804, Bergen, 5020, Norway, Phone: +47 55 58 45 91, Email: Mathias.Ziegler@uib.no.

* These authors contributed equally.

# These authors jointly supervised this work.

Abstract

The coenzyme NAD^+ is consumed by signaling enzymes, including poly-ADP-ribosyltransferases (PARPs) and sirtuins. Aging is associated with a decrease in cellular NAD^+ levels but how cells cope with persistently decreased NAD^+ concentrations is unclear. Here, we show that subcellular NAD^+ pools are interconnected, with mitochondria acting as a rheostat to maintain NAD^+ levels upon excessive consumption. To evoke chronic, compartment-specific over-consumption of NAD^+, we engineered cell lines stably expressing PARP activity in mitochondria, the cytosol, endoplasmic reticulum, or peroxisomes, resulting in a decline of cellular NAD^+ concentrations by up to 50%. Isotope-tracer flux measurements and mathematical modeling show that the lowered NAD^+ concentration kinetically restricts NAD^+ consumption to maintain a balance with the NAD^+ biosynthesis rate, which remains unchanged. Chronic NAD^+ deficiency is well tolerated unless mitochondria are directly targeted. Mitochondria maintain NAD^+ by import through SLC25A51, and reversibly cleave NAD^+ to NMN and ATP, when NMNAT3 is present. Thereby, these organelles can maintain an additional, virtual NAD^+ pool. Our results are consistent with a well-tolerated aging-related NAD^+ decline as long as the vulnerable mitochondrial pool is not directly affected.

Introduction

Among the most versatile biomolecules in all living cells is NAD^+. As a redox factor, it participates in most, if not all branches of metabolism[1-6]. Moreover, in signaling NAD^+ serves as substrate of ADP-ribosyltransferases (ARTs), sirtuins and ADP-ribosylcyclases such as CD38 and SARM1[7-18], and is thus involved in processes ranging from DNA repair, epigenetic and transcriptional control to direct regulation of metabolic enzymes. Common to these signaling reactions is the cleavage of NAD^+, followed by the release of nicotinamide (Nam). For example, PARP1 detects DNA damage and modifies itself and other proteins with polymers of ADP-ribose (PAR) derived from cleavage of NAD^+[19]. These polymers facilitate DNA repair by serving as a molecular scaffold for the DNA repair machinery.

This remarkable array of NAD^+-consuming processes needs to be counterbalanced by NAD^+ biosynthesis. The major route of NAD^+ synthesis in mammals recycles Nam produced in the signaling reactions[20-22]. Nam is converted to nicotinamide mononucleotide (NMN) by nicotinamide phosphoribosyl transferase (NAMPT)[20,21,23,24]. To form NAD^+, NMN combines with the adenylyl moiety of ATP in a reaction catalyzed by NMN adenylyltransferases (NMNATs)[25-27]. In the Preiss-Handler pathway NAD^+ is synthesized from nicotinic acid (NA) via nicotinic acid phosphoribosyltransferase (NAPRT)[28,29]. Common to all pathways is the enzyme NMNAT which catalyzes the formation of the dinucleotide. There are three mammalian NMNAT isoforms that have been localized to the nucleus (NMNAT1), the Golgi complex, facing the cytosol (NMNAT2), and the mitochondrial matrix (NMNAT3) [26,27].

Compartment-specific NAD^+ homeostasis has been highlighted in recent studies as an important determinant of physiological processes such as adipocyte differentiation, neuronal cell survival, metabolic regulation of transcription, and electron transport chain activity [30-35]. The mitochondrial NAD^+ pool appears to be of particular importance to protect cells in stress

situations [36-38]. However, the way in which mitochondrial NAD^+ might contribute to counteract stress originating from other cellular components is not known. The mitochondrial NAD^+ pool has a certain degree of autonomy, which is further indicated by the presence of NMNAT3 within this organelle suggesting the possibility of mitochondrial NAD^+ synthesis [26]. In line with this notion, evidence has been presented suggesting the uptake of NMN or NAD^+ into the organelles [32,39,40]. However, with the recent discovery of SLC25A51, or MCART1, as a mammalian mitochondrial NAD^+ transporter, the molecular basis for the major route of generation of the mitochondrial NAD^+ pool has been established.[41-43] Additionally, NMNAT3 has been demonstrated to be dispensable in mice, further suggesting that this enzyme is not essential for mitochondrial NAD^+ synthesis [44].

Besides the nucleus, cytosol and mitochondria, NAD^+ has also been detected in other subcellular compartments including the peroxisomes and the endoplasmic reticulum (ER) [45,46]. For peroxisomes, a carrier has been described as a possible candidate [47], whereas the route of entry of NAD^+ into the ER remains unknown. A fundamental question therefore relates to the connectivity between the individual NAD^+ pools. To what extent are they autonomous or independent? Does local consumption of NAD^+ remain a local affair or does excessive consumption in one organelle affect other NAD^+ pools? This question becomes particularly relevant in view of the observed decline of tissue NAD^+ content in some diseases such as mitochondrial myopathies [48-51] and, especially, in aging [10,11,52-55]. Decreased NAD^+ contents are most often interpreted to result from excessive NAD^+ consumption or decreased NAD^+ biosynthesis. As a cause for the initial change, this is probably true. However, at equilibrium, synthesis and consumption must have equal rates. Therefore, cause and consequence cannot be readily identified when the change has become stably manifested. In line with this notion, Liu *et al* [56] have established NAD^+ turnover rates in cells and tissues by means of stable isotope

96 labeling and LC-MS based quantification. Using this approach, they were unable to detect
97 changes in NAD^+ turnover in aged mice while NAD^+ concentrations were lowered in most
98 tissues [57].
99 So far, the consequences of NAD^+ depletion on physiological functions have largely been
100 studied through pharmacological blockage of NAMPT, for example, using the inhibitor FK866
101 [36,58-64]. However, this approach is unsuitable to study the consequences of chronically
102 decreased NAD^+ levels, as observed in aging.
103 Here, we present a model system for constitutive, compartment-specific NAD^+ depletion in
104 human cells. Expression of the catalytic domain of PARP1 (referred to as PARP1cd) resulted in
105 significantly lowered total cellular NAD^+ contents, irrespective of the subcellular compartment
106 targeted. NAD^+ depletion was well tolerated provided the mitochondrial pool was not directly
107 affected. The excessive NAD^+-degrading activity did not result in an upregulation of
108 biosynthesis. Thereby, total NAD^+ turnover remained mostly unchanged despite the lowered
109 NAD^+ concentration. Our study thus revealed a demand-dependent kinetic regulation of
110 cellular NAD^+ metabolism and distinct cellular responses to chronically lowered NAD^+ levels
111 that are different from acute NAD^+ depletion.
112 Regardless of the compartment targeted, PARP1cd expression was largely accompanied by a
113 decrease of NAD^+ in mitochondria, indicating a buffering function of this pool. Mechanistically,
114 we propose that NMNAT3, based on its reversibility, maintains a balance between NAD^+,
115 imported by SLC25A51, and NMN (+ATP), which provides a buffer of "NAD^+ equivalents" in
116 addition to mitochondrial NAD^+ itself.
117

118 ## Results

119 **Chronic NAD^+ depletion by stable expression of PARP1cd**

To study the consequences of constitutively diminished NAD^+ levels, we generated cell lines stably overexpressing NAD^+-consuming activity, targeted to different subcellular compartments. Our design was based on the previous demonstration that targeted expression of the PARP1 catalytic domain (PARP1cd) in the cytosol or mitochondria resulted in decreased cellular NAD^+ contents[45,65,66]. We used U2OS, HEK293 (293) and HeLa S3 cells to engineer three sets of cell lines expressing PARP1cd in the mitochondria (mitoPARP1cd or mP), the cytosol (cytoPARP1cd or cP), the peroxisomes (pexPARP1cd or pP) and the endoplasmic reticulum (ER-PARP1cd or erP) (Figs. 1 and Extended Data Fig. 1). PARP1cd, endowed with an N-terminal EGFP-tag, was targeted to peroxisomes by adding a C-terminal SKL targeting signal or to the ER by adding the ER-targeting sequence of Binding immunoglobulin protein (BiP) and the KDEL ER retention signal (Fig. 1a). Cell lines expressing mitochondrial or cytosolic PARP1cd were prepared as previously reported for 293 cells[46]. The resulting proteins consume NAD^+ as a substrate for PAR formation in the targeted compartment [45,46] (Fig. 1b). Expression levels of the PARP1cd construct varied in the different cell lines with a tendency for higher expression levels when targeted to the peroxisomes or the ER. Immunodetection of PAR in the pP cells (Figs. 1c, 1d, and Extended Data Fig. 1a-d), and peroxisomal localization of the PARP1cd construct were confirmed by colocalization with the peroxisomal marker PMP70 (Extended Data Fig. 1d).

In U2OS and HeLa S3 cells stably expressing erP, PAR formation was demonstrated by immunocytochemistry (Fig. 1c and Extended Data Fig. 1a) and Western blotting (Fig. 1d and Extended Data Fig. 1b). In 293 cells stably expressing ER-PARP1cd[45,46], PAR formation was undetectable (Extended Data Fig. 1c and e), while transient expression of the construct resulted in readily detectable PAR[45,46]. We reasoned that PAR degrading activity in the stable 293 erP cells might exceed the speed of PAR generation. If so, increased NAD^+ supply would

144 shift the equilibrium towards PAR accumulation. Indeed, overexpression of nicotinic acid
145 phosphoribosyltransferase (NAPRT) and addition of its substrate, nicotinic acid (NA), to the
146 medium enabled the formation of PAR readily detectable by Western blotting (Extended Data
147 Fig. 1e). The correct targeting of the erP construct was confirmed by colocalization with the
148 ER marker calnexin (Extended Data Fig. 1f).
149 Exploiting PARP1cd as a compartment-specific NAD^+ consumer requires the presence of PAR-
150 degrading activity, that is, a dynamic equilibrium of polymer synthesis and degradation.
151 Otherwise, PARP1cd would be mostly in its maximally PARylated form and inactive. The
152 presence of PAR-degrading activities has been previously verified for mP and cP cells [40,65] and
153 here for erP cells (see above and Extended Data Fig. 1e). PAR degrading activity in peroxisomes
154 was detected by incubating pP cells in presence of the PARP inhibitor 3-aminobenzamide
155 (3AB). Under this condition, the signal for PAR in pP cells weakened in a time-dependent
156 manner (Extended Data Fig. 1g). Pre-incubation of the cells in presence of 3AB for 48 hours
157 followed by release of the inhibition showed that polymer levels were fully restored in the pP
158 cells at 24 hours (Extended Data Fig. 1h). These results verified PAR turnover in all targeted
159 organelles.
160 Next, we validated the suitability of the established PARP1cd cell lines as model systems for
161 chronic NAD^+ depletion. Compared to their parental (wt) counterparts, the total cellular NAD^+
162 contents of PARP1cd-expressing cells were diminished to varying extent in all PARP1cd
163 expressing cells, with the only exception of cP in HeLa cells (Fig. 1e). Expression of PARP1cd in
164 mitochondria and peroxisomes caused the strongest decrease of NAD^+ levels, up to ~50%, in
165 all cell types, while NAD^+/NADH levels were largely unaffected (Extended Data Fig. 1i).
166 Inhibition of PARP activity by 3AB reversed the NAD^+ decrease, even exceeding the level of

untreated wt cells (Fig. 1e). Consequently, NAD^+ depletion upon expression of PARP1cd can indeed be ascribed to the catalytic activity of the constructs.

Only direct mitochondrial NAD^+ depletion is detrimental

Growth rates were largely unaffected by the presence of PARP1cd. Expression of PARP1cd in the peroxisomes, the cytosol or the ER slightly increased growth rates in U2OS PARP1cd cell lines, while expression of cP in 293 and mP in HeLa cells decreased them (Fig. 2a). Next, we evaluated energy metabolism by monitoring mitochondrial respiration and glycolysis based on the oxygen consumption rates (OCR) and the extracellular acidification rates (ECAR, Fig. 2b and Extended Data Fig. 2a and b). Notably, mP cells generated from all backgrounds (U2OS, 293, HeLa S3) displayed substantially lowered basal and maximum (uncoupled) respiration rates, whereas these rates were only somewhat diminished in pP, cP and erP cells (Fig. 2b and Extended Data Fig. 2a and b). Glycolysis was strongly elevated in 293 mP cells (Extended Data Fig. 2a). None of the modified cell lines presented increased leak respiration, indicating that the mitochondrial inner membrane integrity and respiratory control were preserved (Fig. 2b). Consequently, the major bioenergetic functions appear to be well maintained during constitutive NAD^+ deficiency, unless the depletion originates from the mitochondria.

We hypothesized that the constitutive NAD^+ deficiency in the PARP1cd cell lines might be well compensated under resting conditions but forcing them to rely predominantly on oxidative phosphorylation could provoke growth defects. To test this, we measured growth rates in media containing galactose as sole carbon source. Generally, this growth condition resulted in decreased cell proliferation in all cell lines investigated, including the parental cells (Fig. 2c and Extended Data Fig. 2c and d). In 293 cells, PARP1cd expression further decreased proliferation rates irrespective of the compartment targeted.

To further test mitochondrial function in 293 cells, we employed the resazurin assay, which is an indicator of the activity of mitochondrial NAD^+-dependent dehydrogenases[67]. Mitochondrial dehydrogenase activities were maintained in PARP1cd expressing cells regardless of the origin of NAD^+ depletion (Extended Data Fig. 2e). The 293 PARP1cd cells were then challenged with FK866, thereby testing their sensitivity to further NAD^+ depletion based on NAMPT inhibition. Both mP and pP cells were highly sensitive to this condition displaying a marked decrease in signal intensity already after 24 hours with a further decline after 48 hours, whereas cP and erP cells tolerated the treatment for the first 24 hours (Extended Data Fig. 2e). Regarding pP cells, this finding was surprising, as these cells displayed normal oxygen consumption rates.

To compare the sensitivity towards peroxisomal versus mitochondrial NAD^+ depletion, we assessed the functionality of β-oxidation in the 293 PARP1cd cell lines, an NAD^+-dependent process taking place both in peroxisomes (preferential catabolism of long and very long-chain fatty acids) and mitochondria (preferential oxidation of short/medium chain fatty acids) [68]. As shown in Fig. 2d, the mitochondrial NAD^+ depletion in mP cells caused a dramatic accumulation of medium-chain fatty acids, whereas peroxisomal NAD^+ depletion (pP cells) resulted only in a slight increase in very long-chain fatty acids. Since the NAD^+ dependency of peroxisomal and mitochondrial fatty acid oxidation is similar, it appears that peroxisomal NAD^+ depletion is well compensated to maintain oxidation of very-long-chain fatty acids, whereas mitochondrial NAD^+ depletion results in a profound deficiency of β-oxidation.

These results indicated that, despite a considerably lower NAD^+ content in the PARP1cd-expressing cells, metabolic and bioenergetic functions are well maintained, unless the mitochondrial NAD^+ pool is targeted directly. The generally mild effects of chronic NAD^+

depletion were further confirmed by essentially unchanged cellular ATP levels in all PARP1cd expressing cell lines (Extended Data Fig. 2f).

Since sirtuins deacetylate proteins in an NAD^+-dependent manner, changes in cellular NAD^+ levels may affect the acetylation state of a variety of proteins[69-71]. However, no pronounced changes were detectable when comparing protein acetylation in whole cell lysates of wt 293 and 293 PARP1cd cell lines (Fig. 2e). Likewise, the expression of sirtuins was nearly unaffected in 293- and HeLa-derived PARP1cd cells (Extended Data Fig. 2g).

Taken together, the cells coped surprisingly well with constitutive, targeted NAD^+ depletion. These observations indicate that, unlike during acute NAD^+ depletion, cells adapt to chronic NAD^+ deficiency and efficiently maintain physiological functions. However, the pronounced functional deficiencies in mP cells revealed a serious vulnerability when NAD^+ depletion originates from the mitochondrial pool.

NAD^+ turnover does not change upon PARP1cd overexpression

Given the unexpected lack of distinct phenotypical consequences of constitutive NAD^+ deficiency in the majority of PARP1cd cells, we wondered how NAD^+-dependent processes could be maintained, despite the lowered concentration of the dinucleotide. These are stable cell lines that have attained a new balance in NAD^+ metabolism. To establish this equilibrium, an augmented NAD^+ consumption could be counterbalanced by a matching elevation of biosynthesis activity which would result in an increased NAD^+ turnover (Fig. 3a). Alternatively, even though the capacity to degrade NAD^+ is increased in the PARP1cd cells, the actual NAD^+ consumption could be limited, for example, by regulatory mechanisms, to not exceed the available rate of NAD^+ synthesis (Fig. 3a). To distinguish between these possibilities, we determined cellular NAD^+ turnover using stable isotope labeling-based flux measurements.

237 We substituted the respective unlabeled cell culture medium components by ^{13}C glucose and
238 ^{15}N-labeled Nam (for 293-derived cells, Figs. 3b and c and Extended Data Fig. 3a and b) or ^{18}O-
239 labeled Nam for the other cell lines (Extended Data Fig. 4a-d). This approach enables the
240 labeling of NAD^+ in both the Nam and the two ribose moieties (Fig. 3b). Thereby, six different
241 isotopologs can be expected in the measurements (Fig. 3b): unlabeled NAD^+, NAD^+ M+1 (only
242 labeled in the Nam moiety), NAD^+ M+5 (labeled in one of the two riboses), NAD^+ M+6 (labeled
243 both in Nam and one of the two riboses), NAD^+ M+10 (labeled in both riboses) and NAD^+ M+11
244 (labeled in Nam and both riboses).
245 As determined by high-resolution LC-MS, in 293-derived cells, the M+1, M+5 and M+10
246 isotopologs were hardly detectable, independent of the presence of PARP1cd (Extended Data
247 Fig. 3a). Initial accumulation of a M+6 isotopolog was observed, followed by nearly exclusive
248 formation of the M+11 (the fully labeled) isotopolog (Extended Data Fig. 3a). To identify the
249 position of the ribose in the M+6 isotopolog, we used MS-MS fragment analysis. As shown in
250 Extended Data Fig. 3b, a labeled ADP fragment of the M+6 isotopolog was almost absent,
251 whereas the ADP-ribose fragment was completely present in the M+5 form. These findings
252 establish that the first labeled ribose that gets incorporated into NAD^+ is on the NMN, and not
253 the AMP side of the molecule. Consequently, the added ^{13}C glucose must be rapidly converted
254 to ^{13}C PRPP (Fig. 3b), indicating that the cellular PRPP pool is turned over rather quickly. ^{13}C
255 PRPP and ^{15}N Nam are then used by NAMPT to form $^{15}N/^{13}C$ NMN M+6 (Fig. 3b). The final
256 conversion to NAD^+ M+6 is catalyzed by NMNAT, initially using the large pool of unlabeled
257 ATP. Over time, the ATP pool also becomes labeled in the ribose moiety, resulting in the
258 accumulation of NAD^+ M+11. As label incorporation of any sort represents newly synthesized
259 NAD^+, the sum of all detected isotopologs was used to calculate the NAD^+ turnover (Fig. 3b,
260 lower panel, “Sum of labeled NAD^+”). In the steady state, the rate of incorporation of label

into newly synthesized NAD^+ equals the rate of degradation (disappearance) of unlabeled NAD^+ present at time=0 (Fig. 3b, lower panel, "Unlabeled NAD^+"). In other words, the biosynthetic rate equals the consumption rate.

The results of the time-course analyses of NAD^+ labeling in wt 293 and PARP1cd cells are shown in Fig. 3c. The time ($t_{1/2}$) needed to replace 50% of the original, unlabeled NAD^+ pool by newly synthesized, labeled NAD^+ is markedly shortened in the PARP1cd cell lines, in particular, mP and pP cells (Fig. 3c, for the U2OS- and HeLa-derived cell lines, see Extended Data Fig. 4c and d, respectively). Note that these are also the two cell lines whose total NAD^+ concentrations are lowest. Consequently, at similar NAD^+ synthesis rates, it would take less time to resynthesize 50% of their total NAD^+ pool compared to the wt cells. This is visualized in Fig. 3d, in which NAD^+ synthesis is shown in absolute numbers rather than %. Here, the attained maximum of labeled NAD^+ corresponds to the cellular NAD^+ contents, which is approximately half in pP compared to the wildtype. As shown in the bar graphs in Fig. 3e, when scaling to the cellular NAD^+ pool sizes, it becomes obvious that the actual NAD^+ turnover is hardly affected by the expression of the PARP1cd constructs. Consequently, changes in the rates of NAD^+ biosynthesis and consumption in the cells overexpressing the NAD^+ consumer PARP1cd, if any, are rather small. These results argued against a compensatory upregulation of NAD^+ biosynthesis and suggested a kinetic limitation of NAD^+ consumption (Fig. 3a, bottom).

To validate this interpretation, we generated a kinetic model of NAD^+ metabolism to simulate PARP1cd overexpression. As shown in Figure 3f, the model recapitulates the observations of the experiments (Fig. 3d and e) when arbitrarily assuming increases of total maximal NAD^+ consuming activities by 10 or 20% elicited by PARP1cd overexpression. Therefore, both the experimental data and the model suggest that, in the new steady state, maximal consumption

activities cannot be attained owing to a kinetic counterbalancing resulting from lowered NAD^+ concentrations. That is, the K_m values of the NAD^+ consumers (both endogenous and PARP1cd) are in the range of the (free) NAD^+ concentrations in the cell [32,72]. Therefore, a decrease of the NAD^+ concentration will cause a decrease of the overall NAD^+ consumption rate until the biosynthetic rate is matched (Fig. 3g). Assuming an unchanged rate of NAD^+ biosynthesis, increased consumption capacity (yellow line) would cause a decrease of the NAD^+ concentration. Lower enzyme saturation then slows down NAD^+ consumption until degradation and synthesis rates match again to establish a new steady state.

Stable NAD^+ biosynthesis kinetically limits NAD^+ consumption

To consolidate this finding, we analyzed the expression of enzymes involved in NAD^+ biosynthesis. Under the conditions of our experiments, the only available NAD^+ precursor was nicotinamide. Therefore, NAD^+ biosynthesis proceeded via NAMPT and NMNAT, the only intermediate being NMN (Fig. 3b). The amount of NAMPT, as detected by Western blotting, was unchanged in all PARP1cd overexpressing cell lines compared to the parental cell lines (Fig. 4a). Similarly, NMNAT1 protein levels were largely unchanged in U2OS- and HeLa-derived PARP1cd cells and slightly increased in the corresponding 293-derived PARP1cd cells (Fig. 4b). Because it had been reported, at least in 293 and HeLa cells, that changes in *NMNAT* transcript levels correlated with protein abundance[32] we used RNASeq to establish expression levels of the corresponding genes. First, we validated the results obtained from the Western blots for *NAMPT* and *NMNAT1* expression (Fig. 4c). We detected a slight increase in *NAMPT* expression in 293 mP and pP and a decrease in HeLa mP and pP. Given that NAMPT catalyzes the rate-limiting step in NAD^+ synthesis, these results are in accordance with the minor changes observed in NAD^+ turnover (Fig. 3). *NMNAT1* mRNA is slightly increased in HeLa pP and cP and

293 erP (Fig. 4b). In 293 mP cells, *NMNAT3* mRNA levels were increased while *NMNAT2* expression was decreased to a similar extent indicating an interesting compensatory swap from cytosolic to mitochondrial NMNAT activity. In agreement with previous reports[32] *NMNAT2* and *NMNAT3* mRNA levels are extremely low or undetectable in HeLa S3 cells.

Interestingly, a downregulation of *NAPRT* mRNA, in particular in 293 mP cells, was detected (Fig. 4c). NAD^+ biosynthesis from nicotinic acid (NA) through the Preiss-Handler pathway [28,29] is independent of NAMPT (Fig. 4d), and it was previously established that NA can sustain NAD^+ synthesis and cell growth in 293 and mP, when NAMPT is inhibited by FK866 [40]. Indeed, under this condition, NAD^+ is efficiently synthesized from ^{13}C-NA (Fig. 4e) indicating that this pathway is functional and active in the cell lines used in the present study. We reasoned that the PARP1cd cells might increase the use of NA when it is available in the medium to increase NAD^+ concentrations. However, this was not the case. Rather to the contrary, PARP1cd cells, in particular, mP cells, used even less ^{13}C-NA (in addition to the unlabeled Nam in the medium) compared to wt 293 cells (Fig. 4f). In fact, these measurements provided a functional validation of the observed decrease of expression of *NAPRT* in 293 mP, pP and cP cells (Fig. 4c), although the reason for this regulation remains unclear.

Collectively, these results further supported the notion that, independent of the compartment harboring the overexpressed NAD^+ consumer, NAD^+ biosynthesis was not increased to counterbalance the increased NAD^+ consumption. Rather, by maintaining the expression level of *NAMPT*, encoding the rate-limiting enzyme [73], total NAD^+ consumption was limited and mostly unchanged compared to wt cells (cf. Fig. 3a, bottom panel). However, as already noted during the functional characterization, mP cells again stood out with the strongest alterations. Clearly, the constitutive presence of an excessive NAD^+ consumer within mitochondria

affected the cells more severely compared to any other subcellular compartment tested. Therefore, we decided to scrutinize the mitochondrial NAD^+ pool in more detail.

Extramitochondrial consumption lowers mitochondrial NAD^+

As shown in Fig. 5a, mitochondrial NAD^+ levels were decreased in all PARP1cd cell lines derived from wt 293 or HeLa S3 cells as well as mP and pP cells generated from U2OS cells. This result implies an interconnectivity of subcellular NAD^+ pools, suggesting "NAD^+ sharing" of subcellular NAD^+ at least by the mitochondrial pool (Fig. 5a).

As expected, the decrease of NAD^+ in mitochondria was strongest when PARP1cd was expressed within these organelles directly. It was also noted that pP expression consistently evoked a considerable depletion of the mitochondrial NAD^+ pool (Fig. 5a). To validate these measurements, we made use of HeLa cells constitutively expressing a genetically encoded NAD^+ biosensor in mitochondria[32]. Transient expression of the mitochondrial PARP1cd construct in these cells demonstrated a similar decline of the free mitochondrial NAD^+ concentration (Extended Data Fig. 5a) as measured in the organelles isolated from mP cells (Fig. 5a). Moreover, expression of pP in HeLa cells expressing the mitochondrial NAD^+ sensor (Extended Data Fig. 5a-c) confirmed the notion that the mitochondrial NAD^+ pool may be "tapped" in a situation of NAD^+ shortage in other subcellular locations (Fig. 5a).

Dynamics of the mitochondrial NAD^+ pool

Given the consistent draining of the mitochondrial NAD^+ pool upon PARP1cd expression in various extramitochondrial compartments, it seemed surprising that the corresponding PARP1cd cell lines hardly exhibited any functional defects. Therefore, we wondered to what extent the dynamics of the mitochondrial NAD^+ pool might be affected under these conditions. We conducted time course experiments using stable isotope labeling, similar to those shown in Fig. 3, in 293-derived PARP1cd cell lines. To assess the dynamics of the mitochondrial NAD^+

pool, we isolated the organelles and measured isotope incorporation into this pool. Taking into account the cellular and mitochondrial NAD^+ contents (see Materials and Methods for details), we estimate that, in parental 293 cells, mitochondria contribute ~15% to the total cellular NAD^+ turnover (Fig. 5b). In 293 mP cells, mitochondrial NAD^+ turnover was hardly measurable, consistent with the very low remaining NAD^+ concentration (Fig. 5a). Likewise, mitochondrial NAD^+ turnover was somewhat reduced in pP, cP and erP cells. However, this decrease was fairly small with no significant difference from the wt situation. Together, these results demonstrate that increased extramitochondrial NAD^+ consumption may be compensated, in part, by draining the mitochondrial pool whose dynamics remain largely unaffected.

SLC25A51, but not NMNAT3, controls mitochondrial NAD^+ levels

The NAD^+ concentration in mitochondria (~230 µM) is known to be considerably higher than in other compartments, such as the nucleus or cytosol (~100 µM)[32,72], even though the K_m values of the majority of mitochondrial NAD-dependent metabolic reactions are far below this concentration[74]. Consequently, mitochondria might represent a reservoir that could potentially compensate cellular NAD^+ fluctuations. Such a function should be intrinsically linked to the mechanisms underlying the establishment and maintenance of the mitochondrial NAD^+ pool. In mammalian cells, mitochondrial NAD^+ originates from the cytosol and is imported by SLC25A51/MCART1, an NAD^+ carrier in the mitochondrial inner membrane[41-43] (Fig. 5c). We generated 293 cells overexpressing (*A51* OE) or deficient (*A51* KO) in the mitochondrial NAD^+ carrier SLC25A51 (Extended Data Fig. 6a-c). In accordance with previous reports[41,42], the absence of the carrier had little effect on cellular NAD^+ levels (Fig. 5d), whereas mitochondrial NAD^+ was hardly detectable (Fig. 5e). In contrast, overexpression of

SLC25A51 increased cellular NAD^+ contents (Fig. 5e), with a large share of the additional NAD^+ present in mitochondria (Fig. 5e). These observations demonstrate that SLC25A51 controls the mitochondrial NAD^+ content and regulates the distribution between intra- and extramitochondrial NAD^+ pools.

In a variety of cell types, including 293, mitochondria contain NMNAT3, an enzyme that reversibly converts NMN and ATP to NAD^+ and pyrophosphate (Fig. 6a). While nuclear NMNAT1 and cytosolic NMNAT2 are required for NAD^+ synthesis, the function of NMNAT3 in mitochondria has remained elusive.

To understand the role of NMNAT3 in mitochondrial and cellular NAD^+ homeostasis, we used commercially available HAP1 KO cells and generated stable 293-derived cell lines overexpressing (*NMNAT3* OE) or deficient (*NMNAT3* KO) in this protein (Extended Data Fig. 7-9). In contrast to the effects of SLC25A51 modulation, neither overexpression nor knockout of *NMNAT3* had any noticeable effect on cellular or mitochondrial NAD^+ levels (Fig. 6b and c). Moreover, deletion of *NMNAT3* in 293 cells did not alter mitochondrial NAD^+ availability as determined using mitoPARP1cd as a sensor (Fig. 6d and e). The same results were obtained when comparing HAP1 *NMNAT3* KO cells to their wt counterpart (Extended Data Fig. 7a-c). Thereby, we confirm that NMNAT3 is not required for mitochondrial NAD^+ synthesis. Moreover, this enzyme does not directly control mitochondrial or total cellular NAD^+ pools.

The NMNAT3 equilibrium establishes a mitochondrial NAD^+ buffer

The NMNAT-catalyzed reaction is fully reversible [26,75], with the chemical equilibrium favoring the production of NMN and ATP from NAD^+ and pyrophosphate[25,26,76] (Fig. 6a). We hypothesized that NMNAT3 might preferentially work in the direction of NAD^+ cleavage until the equilibrium between NAD^+ + PPi and NMN + ATP is reached. To test this, we first exploited

404 the mitochondrial NAD^+ sensing capacity of mitochondrial PARP1cd[46]. We speculated that, if
405 NMNAT3 preferentially cleaved NAD^+, then the *NMNAT3* KO should have more mitochondrial
406 NAD^+ available for the PARP1cd to produce PAR. As shown in Fig. 6d, no difference in PAR
407 formation by mitoPARP1cd between wt and *NMNAT3* KO 293 cells was detectable.
408 Additionally, in *SLC25A51* KO cells, the very low remaining mitochondrial NAD^+ content (Fig.
409 5f) is undetectable using this assay (Fig. 6f – third lane from the right). Remarkably, if under
410 this condition *NMNAT3* is knocked out as well, PAR becomes detectable, clearly indicating a
411 rise of NAD^+ available to the mitochondrial PARP1cd (Fig 6f, rightmost lane). This observation
412 suggested that NMNAT3 preferentially cleaves NAD^+, thereby competing with PAR generation
413 by PARP1cd. According to this concept, NMNAT3 should produce and thereby elevate the
414 NMN level in mitochondria. Hence, we decided to measure mitochondrial NMN
415 concentrations in the context of *NMNAT3* overexpression or knockout (Fig. 6g). As shown
416 above (Fig. 6c and d), the mitochondrial NAD^+ content is indistinguishable from the wildtype
417 under these conditions. Overexpression of *NMNAT3* did also not influence the mitochondrial
418 NMN concentration (Fig. 6g). Strikingly, knockout of *NMNAT3* reduced mitochondrial NMN
419 concentrations by up to 50% (Fig. 6g). These results show that NMNAT3 can maintain an
420 equilibrium between NAD^+ and NMN that enables accumulation of "NAD^+ equivalents" in the
421 form of NMN (Fig. 6h).
422

423 ## Discussion

424 The present study has provided important new insights into the physiology of intracellular
425 NAD^+ pools, their interconnectivity, dynamics and plasticity. Using the model system of
426 compartment-specific PARP1cd expression, we have identified mechanisms that enable the
427 maintenance of cellular processes under the conditions of chronic NAD^+ depletion.

Surprisingly, the main mechanism relies on “autoregulation”, adjustment of NAD^+ metabolism based on the kinetic properties of the enzymes. The relatively large mitochondrial pool appears to be particularly vulnerable when directly affected, but it may act as a cellular NAD^+ reserve when the shortage originates outside the organelles.

Our experiments indicate that human cells have the capacity to compensate sustained decreases of total cellular NAD^+ contents. Out of the twelve generated PARP1cd cell lines (4 x each U2OS, 293 and HeLa S3), eleven displayed a significantly lower NAD^+ concentration compared to their respective wildtypes (Fig. 1e). Yet, their growth rates were hardly affected. Likewise, challenging the cells with glucose-free medium that contained galactose was well tolerated. However, irrespective of their background (HeLa S3, 293, U2OS), all mP cells exhibited reduced respiratory activity, whereas PARP1cd expression in other compartments had little impact on bioenergetic and metabolic parameters. These observations suggest that human cells are capable of efficiently adjusting their metabolism when encountering prolonged NAD^+ shortage, as long as the origin of the imbalance is located outside mitochondria.

Increased total NAD^+ consumption activity by PARP1cd expression caused a drop of NAD^+ levels in accordance with the kinetic parameters of cellular NAD^+ metabolism. The overall rates of biosynthesis and consumption are brought back into balance by lowering the saturation of NAD^+ consumers, thereby decreasing their activity to again match the rate of NAD^+ synthesis. Accordingly, the original NAD^+ turnover is reestablished, however, for the price of a lowered NAD^+ concentration (Fig. 3g). This conclusion is in line with an unchanged NAD^+ flux in tissues of aged mice, despite a significant decline of NAD^+ levels[57]. Even though our cell models do not account for regulatory processes that may take place on an organismal level, they indicate potentially important mechanistic consequences: (i) The NAD^+

concentration per se is unlikely to represent a suitable parameter to evaluate changes in the total activity of NAD^+-dependent processes. Such an evaluation requires turnover measurements, for example, using isotope labels as shown in this and previous studies[56,57]. (ii) Adaptation to excessive NAD^+ consumption can be described by a purely kinetic model of NAD^+ metabolism pointing towards a lack of cellular switches that re-adjust NAD^+ levels. The only exception seems to be, when the mitochondrial pool is affected directly as indicated by a reciprocal up- and down-regulation of *NMNAT3* and *NMNAT2* expression under these conditions (Fig. 4c). (iii) Lowered NAD^+ levels, for example, originating from PARP1 overactivation in response to accumulation of DNA damage during aging[38,77-79], would kinetically redistribute NAD^+ consumption. NAD^+ would become less available to low-affinity NAD^+-dependent enzymes. This could eventually lead to perturbations both in bioenergetic, metabolic and signaling pathways. (iv) NAD^+ supplementation to replenish cellular levels could result in a turnover exceeding the physiological one, unless the cause of excessive NAD^+ consumption is counteracted directly. Increased NAD^+ turnover would put pressure on biosynthetic resources such as PRPP and ATP. From this perspective, supplementation with metabolites that already have the ribose attached (NR, NMN)[10,80-87] represents a clear advantage over supplementation with the classical vitamin B3 forms, nicotinamide and nicotinic acid[88].

In line with the previously reported importance of intact mitochondrial NAD^+ homeostasis[31,36-38,77-79], we here demonstrate an exceptional sensitivity of mitochondria towards direct NAD^+ depletion. While total cellular NAD^+ content was diminished to a similar extent when PARP1cd was expressed in mitochondria or peroxisomes (Fig. 1e), this had little effect on pP cells, whereas mP cells were noticeably affected.

The mitochondrial NAD^+ pool is maintained through uptake from the cytosol mediated by SLC25A51. Nevertheless, even under conditions when mitochondrial NAD^+ was diminished, directly or indirectly, the expression of this carrier was essentially unchanged (Extended Data Fig. 7d-e). Knockout of *SLC25A51* dramatically decreased mitochondrial NAD^+, whereas the total cellular NAD^+ content was unchanged. Similar observations were made in a system using knock down of the carrier[38]. Conversely, overexpression of the transporter tended to increase cellular NAD^+ levels[41,43], likely by preferred accumulation in mitochondria (Fig. 5d and e)[42,89]. These results suggest that the activity of this carrier can regulate the balance between intra- and extramitochondrial NAD^+ pools.

NMNAT3 expression is tissue- and cell type-specific[26]. For example, it is highly expressed in 293, but undetectable in HeLa S3 cells[26,32]. Moreover, *NMNAT3* gene disruption in mice is not lethal and causes only a mild phenotype[44,90]. Since the mitochondrial NAD^+ pool is maintained by SLC25A51, NMNAT3 is not required for NAD^+ generation, although its *in vitro* NAD^+ synthesis activity is similar to NMNAT1 and 2[26]. It has been speculated previously that NMNAT3 may cleave rather than synthesize mitochondrial NAD^+[75], as NMNATs maintain an equilibrium between NAD^+ + pyrophosphate and NMN + ATP in vitro [25,26,76]. Because of the high NAD^+ demand in the nucleus and cytosol, the balance for NMNATs 1 and 2 is likely in favor of NAD^+ synthesis. In mitochondria, the NAD^+ concentration exceeds that of the nucleus and cytosol[32,91,92]. Moreover, pyrophosphate is readily available[93] and the order of substrate binding of NMNAT3 favors NAD cleavage , unlike in the other two NMNAT isoforms[94]. Indeed, deletion of *NMNAT3* in 293 cells substantially lowered the mitochondrial NMN content (Fig. 6g). Given that ATP is abundant in mitochondria, NMNAT3 can convert NMN to NAD^+ when the concentration of the dinucleotide decreases (Fig.6a). Therefore, by maintaining an

498 equilibrium between NAD^+ and NMN, this enzyme can provide a reservoir of NAD^+ equivalents
499 (as NMN + ATP) to buffer mitochondrial NAD^+ fluctuations (Fig. 6h).
500 The NAD^+ carrier SLC25A51 transports NAD^+ into mitochondria, thereby establishing an
501 equilibrium between the cytosolic and mitochondrial NAD^+ pools. By converting some of the
502 imported NAD^+ into NMN (and ATP), NMNAT3 enables uptake of more NAD^+ than would be
503 possible in its absence.
504 Our results revealed that the mitochondrial NAD^+ pool is "tapped" when NAD^+ demand is
505 excessive in other subcellular compartments. This finding suggests a role of mitochondria in
506 the communication between subcellular NAD^+ pools. Such a role could be mediated by
507 controlled exchange of NAD^+ between mitochondria and the cytosol and further with other
508 compartments and would involve bi-directional NAD^+ transport by SLC25A51 (Fig. 7). When
509 NAD^+ demand outside mitochondria increases, the dinucleotide would be released from the
510 organelles to replenish the depleted compartment. A buffering function of the mitochondrial
511 NAD^+ pool would provide a plausible reason why the NAD^+ concentration in these organelles
512 is significantly higher compared to those measured in the cytosol and the nucleus[32,91,92].
513 Importantly, with the presence of NMNAT3, the capacity of this NAD^+ buffer could be
514 substantially increased (Fig. 6h). Therefore, we posit that, in concert with SLC25A51, NMNAT3
515 may buffer not only intra-, but also extramitochondrial NAD^+ imbalances (Fig. 7). In the case
516 of chronic excessive NAD^+ consumption, this buffering function is compromised due to the
517 permanent shortage of cellular NAD^+. However, upon acute activation of extramitochondrial
518 NAD^+ consumers, a SLC25A51-NMNAT3-based NAD^+ rheostat could protect cells from damage
519 by buffering cellular NAD^+ levels.
520 In conclusion, the findings of the present study provide a plausible mechanistic explanation
521 for the well-tolerated decline of NAD^+ levels in aging. They document a key role of the

mitochondrial pool in cellular NAD^+ homeostasis and inter-organellar communication and suggest a buffering role of these organelles in the adaptation to increased NAD^+ demand. Moreover, the distribution of cellular NAD^+ resources appears to be governed by kinetic properties, in particular the affinity of NAD^+-dependent enzymes, rather than other regulatory mechanisms. Therefore, an important benefit of therapeutic approaches adjusting declined NAD^+ levels could consist in the re-allocation of the dinucleotide to critical low-affinity NAD^+-dependent processes. Finally, the vulnerability of cells towards direct depletion of their mitochondrial NAD^+ pool highlights an important, hitherto unexplored aspect: NAD^+ decline may arise from different subcellular locations. However, when originating from mitochondria, it could represent a serious pathogenetic factor, for example, in aging-associated diseases.

Methods

Cell culture

Cells were cultivated at 37 °C in humidified atmosphere with 5% CO_2 (standard culture conditions) in Dulbecco´s modified Eagle's medium supplemented with 10% (v/v) fetal calf serum (FCS), 2 mM glutamine, and 1x penicillin-streptomycin (U2OS 293, [HEK-293], HeLaS3) or 1x penicillin-streptomycin (HAP1).

293, U2OS and HeLaS3 cells were obtained from the American Type Culture Collection (ATCC) and their identities confirmed by in-house genotyping using a 3500 Genetic Analyzer (Applied Biosystems/Hitachi) with GlobalFiler™ PCR Amplification Kit (ThermoFisher/Applied Biosystems #4476135) and GeneScan™ 600 LIZ™ dye Size Standard v2.0 (ThermoFisher/Applied Biosystems #4408399). Wild type and *NMNAT3* knock-out HAP1 cells were obtained from Horizon (Supplementary Tab. 1).

Transfections were done using X-tremeGENE™ 9 transfection reagent (Merck/Sigma). Stably transfected cell lines were generated after two rounds of clonal selection in presence of 550 µg/ml G418 for 293 cells and 800 µg/ml G418 for U2OS and HeLa S3 cells and were maintained accordingly.

CRISPR-Cas9-mediated genome editing

CRISPR-Cas9-mediated genome editing in 293 cells was done following the guidelines published by Ran et al. (2013)[95] using plasmid pSpCas9(BB)-2A-Puro (PX459) V2.0 obtained from Addgene (#62988). One day post transfection of 800,000 cells in 6-well plates, about 5% of the transfected cells were transferred to 10-cm dishes and incubated with 2 µg/ml puromycin for 48 h. After 4-6 days, cells were picked and expanded. Cells were assayed for genome-editing at gDNA and cDNA level by Sanger-sequencing of gel-purified PCR and RT-PCR products covering the targeted regions. Genome-editing of HAP1-*NMNAT3*-KO cells (Horizon Discovery HZGHC006367c011) was assayed accordingly.

Transcriptome profile analysis

The analysis of the cell transcriptome profile from total RNA isolated from 3x $5x10^6$ cells after poly-A enrichment was done by Novogene (UK) Co. Differential gene expression analysis and statistical significance evaluation were performed using the DESeq2 method [96].

Cell proliferation and cell confluency measurements

For assessment of growth and Galactose sensitivity in HeLa S3 and U2OS cell lines, 5000 cells per well were seeded in the cavities of 96-well plates, 27 000 cells per well were seeded in triplicate in poly-L-lysine coated 24-well plates. The following day, the cells were washed with

PBS and incubated in glucose-free DMEM (Themo Fisher) supplemented with 10% (v/v) dialysed fetal calf serum (FCS), 2 mM glutamine, and 1x penicillin-streptomycin, 10 mM Glucose or 10 mM Galactose, +/- 3AB. Every 2-3 h, 100x magnified phase contrast images were acquired within 5 days using Incucyte® Live-Cell Analysis System (Sartorius). Images were analyzed for confluency, and growth rates were calculated from the acquired confluency data.

Determination of growth rates

Growth rate estimations were conducted by fitting the data to a logistic function ($\frac{L}{1+e^{-k(x-x_0)}}$), where L represents the upper asymptote, k is the growth rate, x_0 is the inflection point, and e is the base of the natural logarithm. The SciPy [97] optimization function for curve fitting was used to obtain the best-fit curve that captures the underlying growth dynamics.

Resazurin-based *in vitro* toxicology assay

To assess mitochondrial NAD-dependent dehydrogenase activity, a resazurin-based *in vitro* toxicology assay kit was used (Sigma) with incubation time of 2 h. For assessment of FK866 sensitivity, 10,000 cells per well were seeded in 96-well plates and treated with either FK866 (2 µM), FK866 (2 µM) and 3AB (1 mM) or DMF for the indicated time points. A BMG LabTech FLUOstar Optima plate reader (540/10 nm excitation filter/590 nm emission filter) was used for fluorescence detection.

Protein determination, SDS-PAGE and Western blot analysis

Cells were washed with PBS and lysed in 20 mM Tris-HCl (pH 7.4), 1 mM EDTA, 2% (w/v) SDS, 150 mM NaCl, and 1 mM 3AB and the lysate passed ten times through a 23 gauge needle. Protein concentration was determined using BCA reagent (Thermo Fisher Scientific, Pierce).

SDS-PAGE and immunoblot analyses were performed according to standard procedures. Enhanced chemiluminescence (SuperSignal West Dura and SuperSignal West Pico PLUS, ThermoFisher Scientific, Pierce) was used for immunodetection. Images were acquired using a ChemiDoc XRS+ and ImageLab software (Bio-Rad).

Immunocytochemistry

Cells were grown on (optionally, poly-L-lysine-coated) coverslips and fixed for 15 min with ice-cold 4% (w/v) paraformaldehyde in PBS. After 15 min permeabilization with 0.5% (v/v) Triton X-100 in PBS and blocking with complete medium for 1 h, primary antibodies (see Supplementary Tab. 1) diluted in complete medium were added to cells followed by overnight incubation at 4 °C. After washing with PBS and PBS-T (PBS with 0.1% (v/v) Triton X-100), 1 h-incubation with AlexaFluor- secondary antibodies in complete medium at RT and 10 min DAPI-staining, the slides were washed with PBS and PBS-T prior to mounting onto slides. Images were acquired using a Leica TCS SP8 STED 3x confocal laser scanning microscope equipped with a ×100 oil immersion objective (numerical aperture 1.4).

Measurement of mitochondrial respiration and glycolysis

Oxygen consumption (OCR) and extracellular acidification rates (ECAR) were measured using the Seahorse XFe96 Analyzer (Agilent, Santa Clara, CA, US) following the experimental procedure described in detail by VanLinden et al. (2015)[66]. All data were normalized to protein content using BCA reagent or to cell confluency as determined by the Incucyte® Live-Cell Analysis System (Sartorius).

Fatty acids analyses

Fatty acids were quantified as fatty acid methyl esters (FAMEs) by gas chromatography (GC). Cells were grown to confluency in 15 cm dishes. Following trypsinization, the cells were collected in 8 ml fresh medium and centrifuged at 350 x g for 5 min. The pellet was washed with 5 ml PBS, followed by a second centrifugation after which the pellet was resuspended in 200 µl PBS. The samples were stored at -20 °C in nitrogen atmosphere. Prior to analysis, 100 µl internal standard (C21:0 FAME dissolved in isooctane, c = 0.1956 mg/ml) were added to the samples and fatty acids were derivatized to FAMEs by direct esterification with methanolic HCl as described by Meier, et al. [98]. The extracts were diluted 1:5 with isooctane before analysis by gas chromatography. FAMEs were analyzed on a 7890 gas chromatograph (Agilent) equipped with split-splitless injector, flame ionization detector and a BPX70 capillary column (SGE, Ringwood, Australia) as previously described with minor adjustments to the temperature program [99,100]. Identification and quantification were performed in Chrombox C (www.chrombox.org) based on templates from previous analyses of human serum and plasma by gas chromatography coupled to mass spectrometry [101]. Chromatographic areas were corrected by empirical response factors based on the reference mixture GLC-793 (Nu-Chek Prep.) that was run as every 6th sample in the analytical sequence.

NAD^+ biosensor calibration

NAD^+ biosensor calibration was performed according to the method established by Cambronne et al. (2016)[32]. Data collection was conducted on a BD LSRFortessa using 407-F (ex. 407 nm, em. 525/50 nm BP filter) and 488-C (ex. 488 nm, em. 530/30 nm BP filter) for sensor fluorescence intensity, and 561-E (ex. 561 nm, em. 582/15 BP filter) for PI fluorescence intensity. Cells were gated to exclude debris, followed by standard doublet exclusion (Extended Data Fig. 5b panel 1 and 2), and at least 10,000 cells were collected per sample.

Data analysis was conducted using the FlowJo X software with debris and doublet exclusion followed by determination of the geometric mean of the fluorescence intensity. Ratiometric 488/405 nm fluorescence values from the sensor were normalized to the fluorescence from the corresponding cpVenus control. Values from 3-5 independent experiments were fit to a sigmoidal regression model using GraphPad Prism 8 (y=min+[(min−max)/(1+10$^{(logEC50-x)\times HillSlope}$)]) with a 95% confidence interval (Extended Data Fig. 5c).

Quantification of mitochondrial free NAD$^+$ using the cpVenus-based biosensor

200,000 HeLa cells that stably express either the NAD biosensor or the cpVenus control[32] were seeded in 6-well plates. After one day, the cells were transfected with red fluorescent PARP1cd constructs (mKate2-PARP1cd-SKL or MTS-mKate2-PARP1cd-myc) in the absence or presence of 1 mM 3AB. Alternatively, cells were incubated with 2 µM FK866 or its solvent DMF. After 48 hours, the cells were analyzed using a BD LSRFortessa with a 407-F (ex. 407 nm, em. 525/50 nm BP filter) and a 488-C (ex. 488 nm, em. 530/30 nm BP filter) for sensor fluorescence intensity, and 561-E (ex. 561 nm, em. 661/20 BP filter) for mKate2 fluorescence intensity. Further processing was done as described above. The change in concentration between positively and negatively transfected cells was calculated in percent for each sample. Alternatively, the change in concentration upon treatment with FK866 was calculated in percent compared to the solvent control.

Synthesis of the ^{15}N-Nam and ^{18}O-Nam

The ^{15}N-Nam and the ^{18}O-Nam were synthesized as described previously[102,103].

Generation of ^{13}C-^{18}O – labeled standard from HeLa S3 cells

HeLa S3 cells were incubated with custom made glucose-, pyruvate-, glutamine-, pantothenic acid-, nicotinamide and phenol red-free DMEM DMEM (Cell Culture Technologies) supplemented with 10% dialyzed serum (Gibco, Fisher Scientific), 1 x penicillin/streptomycin, 2 mM L-glutamine, 33 µM ^{18}O-Nam and 25 mM ^{13}C-6 D-glucose (Cambridge Isotope Laboratories Inc.). The medium was replaced after 24 h. After 48 h of incubation with the labeled compounds, the medium was removed, the cells washed twice with PBS and lysed in 8 ml ice-cold 80% (v/v) LC-MS grade methanol (VWR). The sample was scraped from the dish and transferred to 50 ml tubes. Plates were washed with 5 ml ice-cold 80% (v/v) LC-MS grade methanol and the pooled samples stored at -80 °C. After one day, the samples were vortexed (20 sec), centrifuged (4°C, 3000 x g, 10 min) and the supernatant was aliquoted into 1.5 ml tubes. For quantification, unlabeled metabolites with known concentrations were co-injected.

Generation of ^{18}O-NMN

Human NAMPT was expressed and purified as described previously [104]. Upon overnight incubation of 100 µg purified human NAMPT in the presence of 1 mM ^{18}O-Nam, 1 mM PRPP (Sigma) in 1 mL 50 mM Tris-HCl pH 8.0, 300 mM NaCl, 5 mM $MgCl_2$, the samples were filtered (Amicon Ultracel, 0.5 ml, 10 kD cut off). The flowthrough was collected and stored at -80°C. The identity was confirmed by the co-elution with authentic (unlabeled) NMN and the detected m/z value corresponding to the theoretical value. For determination of cellular and mitochondrial NMN levels, 3 µL of ^{18}O NMN were mixed with 12 µL of sample.

Isotopic labeling, nucleotide extraction and LC-MS analysis

688 250,000 cells were seeded in 12-well plate and incubated overnight. Isotopic labeling using
689 ^{13}C glucose (Cambridge Isotope Laboratories Inc.), $^{15}N/^{18}O$ nicotinamide or ^{13}C nicotinic acid[102]
690 was performed as follows: The medium was exchanged with 1 ml custom made glucose-,
691 pyruvate-, glutamine-, pantothenic acid-, nicotinamide and phenol red-free DMEM (Cell
692 Culture Technologies) supplemented with 10% dialyzed serum (Gibco, Fisher Scientific), 1x
693 penicillin/streptomycin, 2 mM L-glutamine, 33 µM Nam (Sigma/Merck), and 25 mM D-glucose
694 (Sigma/Merck). On the next day (T0) the medium was exchanged with 1 ml custom made
695 medium containing the labeled compounds at corresponding concentrations and samples
696 were collected at the indicated time points.
697 For sample collection, cells were placed on ice, the medium was removed, and the cells were
698 washed twice with 0.4 ml ice-cold PBS. Then 0.4 ml ice-cold 80% (v/v) methanol were added,
699 the samples scraped from the wells and transferred to 1.5 ml tubes. This was repeated with
700 0.3 ml methanol and the sample frozen at -80 °C. For LC-MS measurements 420 µL ice-cold
701 Millipore H_2O, and 700 µL ice-cold chloroform (HPLC Plus, Sigma) were added, the samples
702 vortexed for 10 sec and centrifuged for 30 min at 16000 x g at 4˚C. 600 µL of the polar upper
703 phase was transferred to a fresh Eppendorf tube, dried, and reconstituted in 50 µL ice-cold
704 80% (v/v) LC-MS grade methanol. The remaining inter- and lower phase were dried, the pellet
705 was lysed in 20 mM Tris-HCl (pH 7.4), 1 mM EDTA, 2% (w/v) SDS, 150 mM NaCl, and the
706 protein content was determined by BCA assay for normalization of the measured metabolites.
707 Separation of nucleotides by liquid chromatography was achieved on an Atlantis Premier BEH
708 Z-HILIC VanGuard FIT Column (100 x 2.1mm, 100 Å, 2.5 µm, Merck) in a Dionex UltiMate 3000
709 UPLC system coupled with a QExactive mass spectrometer (Thermo Scientific). For analysis,
710 the column was kept at 40 °C, the injection volume was 10 µl, and the flow rate 0.3 ml/min
711 for total run time of 16 min. The mobile phase consisted of 3% acetonitrile, 10 mM NH_4HCO_3,

pH 8.75 (buffer A) and 90% acetonitrile, 10 mM NH_4HCO_3, pH 8.75 (buffer B). The gradient was set as follows: runs were started with 94.4% buffer B for 1 min and reduced to 81% buffer B over the next 5 min. The concentration of buffer B was further decreased to 65% over an additional 5 min before being brought to 30% over 4 min for washout. For equilibration, the concentration of buffer B was returned to 94.4% over 2 min.

Heated electrospray ionization (H-ESI) and positive ion polarity mode were used (spray voltage of 3.5 kV, flow rates: sheath gas 48 units, auxiliary gas 11 units, sweep gas 2 units). The capillary temperature was 256°C and the auxiliary gas heater temperature was 413°C. The stacked-ring ion guide (S-lens) radio frequency (RF) level was at 30 units. Automatic gain control was set to 2E5 ions and the maximum injection time was 200 ms. Ions were monitored in Full MS and targeted single ion monitoring (t-SIM) modes with a resolution of 70000 at m/z = 200. The Full MS spectra ranges were 80-400 and 400-1000 m/z while the t-SIM mass range was set to 671±20 m/z. Data analysis was conducted in the Thermo Xcalibur Quant Browser (Thermo Scientific).

Isolation of mitochondria from cultured human cells

Isolation of mitochondria form cultured human cells was carried out using the MidiMACS® mitochondria isolation kit (Miltenyi Biotech) following manufacture description. The resulting pellet was either resuspended in 100 µl lysis buffer (20 mM Tris-HCl pH 7.4, 150 mM NaCl, 2% (w/v) SDS, 1% (w/v) EDTA) for immunoblot analysis, or in ice-cold 80% (v/v) LC-MS grade methanol and immediate transfer to -80 °C for LC-MS analysis. For LC-MS analysis, the samples were thawed for 30 min on a rotating wheel at 4 °C before centrifugation at 16,000 x g for 20 min at 4 °C. After centrifugation, the supernatant was removed and added to 1 volume of acetonitrile prior to analysis. The samples were further mixed in a ratio of 1:5 with an internal

736 ^{13}C-labeled standard for the accurate determination of the NAD$^+$ concentration. The samples
737 were subsequently analyzed by LC-MS analysis as described above.
738
739 **Isotopolog Correction**
740 To correct for natural isotope abundance the python package PICor v1.1.0
741 (https://github.com/MolecularBioinformatics/PICor) was used[105].
742
743 **Growth correction**
744 The isotopolog-corrected ratios of labeled to total NAD over time (t) were corrected for the
745 changes in the cellular NAD abundance as per Equation 1.

746 $$\left(\frac{NAD_{label}}{NAD_{total}}\right)' = \frac{NAD_{label}/NAD_{total}}{1 + k \cdot t}, \quad (1)$$

747 where k is the growth rate estimated by fitting an exponential function ($A \cdot e^{k \cdot t}$) to the
748 measured total NAD over time t. The SciPy[97] optimization function for curve fitting was used.
749 The associated standard error was calculated as the square root of the diagonal elements of
750 the covariance matrix ($\mathrm{Cov}(\beta)$) of parameters $\beta = \{A, k\}$. The covariance matrix of
751 parameters β is given by

752 $$Cov(\beta) = \sigma^2(\mathbf{J}^T\mathbf{J})^{-1}. \quad (2)$$

753
754 Here, $\mathbf{J}$ is the Jacobian matrix of the exponential decay function with respect to the parameters
755 β. The matrix $\mathbf{J}$ is

756 $$\mathbf{J}_{i,j} = \frac{\partial f(t_i;\beta)}{\partial \beta_j} \quad (3)$$

757 and

$$\sigma^2 = \frac{S(\beta)}{n-p}. \quad (4)$$

Here, each element of $\mathbf{J}$ represents the partial derivative of the function with respect to the j^{th} parameter, evaluated at the i^{th}data point. $S(\beta)$ is the sum of squared residuals evaluated at the optimal parameters, n is the number of data points, and p is the number of parameters.

Determination of cellular half-life and turnover rates

The half-life ($t_{1/2}$) of NAD was estimated based on fitting an exponential decay function to the measured ratios of unlabeled to total NAD over time (t) (cf. Equations 5 and 6). The SciPy[97] optimization function for curve fitting was used for determining the prefactor A and the exponential factor k. The respective standard errors were determined by taking the square root of the diagonal elements of the parameters' covariance matrix, as outlined in the previous section.

$$t_{1/2} = \frac{\ln(2)}{k} \quad (5)$$

$$\frac{NAD_{unlabelled}}{NAD_{total}} = A \cdot e^{-kt} \quad (6)$$

The turnover (τ) and the associated standard error (ε_τ) were determined using Eq. 7-8, respectively.

$$\tau = \frac{C_{NAD}/2}{t_{1/2}} \quad (7)$$

$$\varepsilon_\tau = \tau \cdot \sqrt{\left(\left(\varepsilon_{C_{NAD}}/C_{NAD}\right)^2 + \left(\varepsilon_{t_{1/2}}/t_{1/2}\right)^2\right)}. \quad (8)$$

Here, C_{NAD} corresponds to the NAD pool size and $\varepsilon_{C_{NAD}}$ denotes the standard deviation in the pool size measurement.

Determination of mitochondrial half-life and turnover rates

The whole cell and mitochondrial half-lives were estimated by fitting the respective labeling dynamics to the exponential decay function (Eq. 6). The extramitochondrial (*emito*) labeling dynamics were determined by calculating the difference between the whole cell (*wcl*) and mitochondrial (*mito*) labeling dynamics using Equation 9.

$$\frac{NAD_{unlabeled,emito}}{NAD_{total,emito}} = C_{NAD,wcl} \cdot \frac{NAD_{unlabeled,wcl}}{NAD_{total,wcl}} - C_{NAD,mito} \cdot \frac{NAD_{unlabeled,mito}}{NAD_{total,mito}}. \quad (9)$$

The estimated subcellular half-lives and the subcellular NAD abundances were used to determine the extramitochondrial and mitochondrial turnovers as τ_{emito} and τ_{mito}, respectively, as per Eq. 7.

Model simulations

To simulate the label integration in cell lines in a steady state situation, we created a mathematical model including a reaction for NAD consumption connected to NamPT and NMNAT to simulate the biosynthesis and consumption cycle. Only the major isotopologs were included, assuming instant labeling of glucose, Nam and PRPP. Competition between different isotopologs was simulated using competitive binding in random irreversible bimolecular reactions as described earlier [106]. In addition, ATP synthesis and degradation were simulated using mass action kinetics to be able to resemble the dynamic behavior of all major NAD isotopologs. To simulate the individual enzyme kinetics, the respective substrates and

products were set as external. This simulates the action of enzymes in isolation. Copasi 4.29[107] was used to perform all simulations.

Statistical analyses

Statistical analyses were performed using GraphPad prism version 10. Unless stated otherwise, data from all experiments were analyzed with one-way ANOVA. Due to the heterogeneity of variance, we applied Welch's ANOVA followed by Dunnett's T3 multiple comparisons test as a post hoc analysis.

The statistical significance of the estimated turnovers was assessed by computing the t-statistic based on the turnover (sample mean) and standard error (estimated from the standard deviation). Subsequently, the p-value was derived from the cumulative distribution function of the t-distribution, taking into account the relevant degrees of freedom[108]. Scipy[97] statistical functions were used for these calculations.

Data availability

All data are available within the manuscript, extended data, source data files or supplementary files. RNA sequencing data have been deposited in GEO under accession code GEO GSE255209.

Code availability

Scripts used to produce figures presented in this manuscript can be downloaded from GitHub: https://github.com/MolecularBioinformatics/NADpools. The mathematical model is available at https://www.ebi.ac.uk/biomodels/MODEL2409150001 .

Acknowledgements

We acknowledge funding by the Norwegian Research Council (315849 and 325172) to MZ, IH and ØS. In addition, this work was supported by the Translational Research Institute through NASA Cooperative Agreement NNX16AO69A. We also thank the Mitchell Cancer Institute for its support.
All imaging was performed at the Molecular Imaging Center (MIC), Department of Biomedicine, University of Bergen. The flow cytometry was performed at the Flow & Mass Cytometry Core Facility, Department of Clinical Science, University of Bergen. The computations were partially performed on resources provided by UNINETT Sigma2–the National Infra-structure for High Performance Computing and Data Storage in Norway.
We thank Roberto Megias for supporting the initial LC-MS analyses, Eugenio Ferrario for the synthesis of ^{18}O-NMN and Ana Rita Guillot Caldas who helped with the generation of CRISPR-engineered cells.
Figures 1a and 1b as well as the right panel in Figure 5a were created in BioRender. Høyland, L. (2024) BioRender.com/d01t589.

Author contributions

IH and MZ conceived the project. MZ, IH, LEH, MvL, MN, KJT, SAM and MEM designed experiments. LEH, MvL and MN performed most of the experiments. Work with cell lines was also conducted by ØS, IT, LJS, CCW, HA, KFH, BvdH, ChD and IKNP. FH and MVM conducted chemical syntheses. EL, EB, LEH and LJS performed LCMS analyses. JD and SS carried out data processing and isotope corrections. SS, LEH and CeD conducted statistical analyses, IH performed mathematical modeling. SAM measured esterified fatty acids. All authors analyzed data. LEH, MvL, IH and MZ wrote the manuscript.

Competing interests

M.Z. is chief scientist at Blue Helix Health AS. All other authors declare no competing interests.

Figure Legends

Figure 1: Chronic depletion of cellular NAD^+ by stable expression of PARP1 catalytic domain (PARP1cd) in various subcellular compartments

a) Illustration of poly-ADP-ribosyltransferase 1 (PARP1) and PARP1 catalytic domain (PARP1cd) fusion proteins targeted to the cytosol, the peroxisomes, the mitochondria, or the endoplasmic reticulum (ER). BIP - ER targeting signal, EGFP - enhanced green fluorescent protein, KDEL - ER retention sequence, MTS - mitochondrial targeting

sequence, myc - myc-epitope, NLS - nuclear localization signal, SKL - peroxisomal targeting sequence.

b) Constitutive expression of PARP1cd fusion proteins in the compartment of interest results in the generation of poly-ADP-ribose (PAR).

c) Confocal fluorescence micrographs of U2OS PARP1cd cell lines. PAR was detected by indirect immunocytochemistry using the PAR (10H) antibody, red; DAPI staining, blue; EGFP, green. Scale bar 20 µm.

d) PAR immunoblot analysis of lysates from parental U2OS (wt) and U2OS PARP1cd cell lines. Proteins from the same experiment were loaded on two different gels (PAR and GAPDH, EGFP). Results shown are representative of three repetitions.

e) Total cellular NAD^+ content in PARP1cd cell lines generated from wt U2OS, HeLa S3 and 293 cells as determined by LC-MS analysis. Measurements were performed in presence or absence of 3-aminobenzamide (3AB, 1 mM, 48h). Results were normalized to protein content and data are represented relative to the respective wt cell lines. Data are expressed as the mean ± SD, n = 3-12 biological replicates (293: n = 6 for wt and mP, n = 5 for pP, remaining conditions n = 3; U2OS: n = 12 for wt and wt + 3AB, remaining conditions n = 9; HeLa S3: n = 12 for wt, remaining conditions n = 9). Statistical significance was evaluated by Brown-Forsythe and Welch ANOVA test in combination with Dunnetts T3 as post hoc test.

Illustrations in a) and b) were generated with BioRender (https://biorender.com).

Figure 2: Chronic NAD^+ depletion is well tolerated by human cells unless the mitochondrial pool is directly affected

a) Growth rates of U2OS, 293 and HeLa S3 PARP1cd cell lines. Data are represented as mean ± SD with n ≥ 3. biological replicates (293: n = 20, n = 5 for cP and erP, n = 4 for mP, n= 3 for pP; U2OS: n = 3 for mP, remaining conditions n = 6; HeLa S3: n = 3).

b) Oxygen consumption rates (OCR) in U2OS PARP1cd cell lines and compared to parental U2OS (wt) cells. Data are presented relative to U2OS wt cells as mean ± SD with n = 9 biological replicates for wt cells and n = 3 for PARP1cd cell lines.

c) Proliferation of U2OS PARP1cd cells during 96 h of incubation with galactose as the sole carbon source. Data are presented relative to the proliferation of the same cell lines grown in glucose as means ± SD, where n = 3 biological replicates.

d) Relative cellular abundance of fully saturated fatty acids in stably transfected PARP1cd cell lines compared to parental 293 (wt) cells as determined by gas chromatography coupled to mass spectrometry. All data are expressed as the mean ± SD with n = 9 biological replicates for wt cells and n = 3 for PARP1cd cell lines.

e) Overall lysine (Kac), tubulin and histone acetylation as determined by immunoblot analysis of lysates from parental 293 cells and stably transfected PARP1cd cell lines. Expression of PARP1cd proteins was confirmed by detection of their EGFP tags, while α-tubulin served as loading control. Results shown are representative of three independent repetitions.

For a)-d) statistical significance versus wt was evaluated by one-sided Brown-Forsythe and Welch ANOVA test with Dunnetts T3 as a post hoc test. mP – mitoPARP1cd, pP – pexPARP1cd, cP – cytoPARP1cd, erP – erPARP1cd.

Figure 3: NAD^+ turnover does not change upon PARP1cd overexpression

Graphic summary of the alternatives of how NAD^+ synthesis and consumption could be balanced in response to increased NAD^+ consumption capacity in PARP1cd cell lines.

a) Schematic representation of the metabolic labeling approach to determine NAD^+ turnover. Cells were incubated with isotopically labeled nicotinamide (^{15}N, red) or glucose (^{13}C, blue), allowing for labeling in both the Nam moiety and the ribose moieties (upper panel). The time-dependent appearance of labeled isotopologs is accompanied by the disappearance of unlabeled NAD^+. Here shown for 293 wt cells where n = 6 biological replicates (lower panel).

b) Time courses of label incorporation into NAD^+ in 293 (wt) and 293 PARP1cd cell lines. The half-life was calculated using the fitted exponential decay of the unlabeled NAD and corresponds to the time point when 50% of NAD^+ is labeled (dashed line) and 50% unlabeled (solid line), n = 6 biological replicates

c) Time courses of NAD^+ labeling in 293 wt and PARP1cd cell lines. The attained maximum corresponds to the total NAD^+ concentration in the respective cell line. Data are presented as means ± SD where n = 6 biological replicates.

d) NAD^+ turnover of parental (wt) 293, U2OS, HeLa S3, and the corresponding PARP1cd cell lines. Data are presented as means ± SD where n = 9 biological replicates. Statistical significance versus wt was evaluated by calculating the t-statistic (two-sided). The p-value was estimated from the cumulative distribution function of the t-distribution.

e) Simulations of NAD^+ labeling time courses using a mathematical model of NAD^+ biosynthesis and consumption. PARP1cd overexpression was simulated by increasing the maximal velocity (capacity) of NAD^+ consumption while keeping the maximal velocity of NAD^+ biosynthesis constant.

f) Demand-supply model showing the dynamics of NAD^+ consumption and biosynthesis. To achieve steady state, both processes must balance each other. The intersections therefore represent the theoretical steady state concentrations of NAD^+, reflecting the kinetic balancing effect that leads to decreased NAD^+ concentration upon overexpression of PARP1cd (simulated as 20% increased consumption capacity).

mP – mitoPARP1cd, pP – pexPARP1cd, cP – cytoPARP1cd, erP – erPARP1cd.

Figure 4: Unchanged NAD^+ biosynthesis kinetically precludes NAD^+ overconsumption in PARP1cd cell lines

a) NAMPT in PARP1cd cell lines compared to wt 293, U2OS or HeLa S3 cells as analyzed by Western blotting. GAPDH and β -tubulin served as loading controls. Results shown are representative of three repetitions.

b) NMNAT1 in PARP1cd cell lines compared to wt 293, U2OS or HeLa S3 cells as analyzed by western blotting. GAPDH and β -tubulin served as a loading controls. Results shown are representative of three repetitions.

c) Expression levels of genes encoding NAD biosynthetic enzymes in 293- and HeLa S3-derived PARP1cd cell lines relative to the corresponding parental cells. Gray color indicates that changes, if any, were not significant.

d) Schematic representation of the Preiss-Handler (starting from nicotinic acid, NA) and the salvage NAD^+ biosynthetic pathways. The red color indicates the ^{13}C label in NA used for the experiments shown in panels e) and f).

e) Distribution of NAD^+ labeling following 48 hours of incubation of 293 wt cells and 293 PARP1cd cell lines in presence of ^{13}C-labeled NA and FK866 (2mM). Data are presented relative to parental 293 (wt) cells as mean ± SD where n = 3 biological replicates.

f) Distribution of NAD^+ labeling following 48 h incubation of parental 293 cells and stably transfected PARP1cd cell lines in the presence of ^{13}C-labeled NA. Data are presented relative to parental 293 (wt) cells as mean ± SD where n = 3 biological replicates.

For e) and f) statistical significance was evaluated by Brown-Forsythe and Welch ANOVA test in combination with Dunnetts T3 as a post hoc test.

mP - mitoPARP1cd, pP – pexPARP1cd, cP – cytoPARP1cd, erP – erPARP1cd.

Figure 5: The mitochondrial NAD^+ pool is regulated by SLC25A51 and is diminished in PARP1cd cell lines, irrespective of PARP1cd location

a) NAD^+ contents in mitochondria isolated from stably transfected 293, HeLa S3, or U2OS PARP1cd cell lines. Results were normalized to protein concentration, and data are represented relative to the respective wt cells as mean ± SD where n = 3 biological replicates (except for HeLa S3 mP and cP where n = 4). Right panel: A proposed model in which mitochondrial NAD^+ is provided to other subcellular compartments upon increased NAD consumption.

b) Relative contributions of extramitochondrial and mitochondrial NAD^+ turnover to total cellular NAD^+ turnover in 293 wt and cell lines. Metabolic labeling was conducted as described for Fig. 3, and turnovers were calculated taking into account the subcellular NAD^+ distribution.

c) Schematic representation of mitochondrial NAD^+ transport via the mitochondrial NAD transporter SLC25A51.

d) Total cellular NAD^+ content in 293 *SLC25A51* KO (*A51* KO) and stable *SLC25A51* overexpressing (*A51* OE) cells as determined by LC-MS analysis following methanol

extraction. Results were normalized to protein content and data are represented relative to the respective wt cells as mean ± SD where n = 3.

e) Total NAD^+ content in mitochondria isolated from 293 *SLC25A51* KO (*A51* KO) and stable *SLC25A51* overexpressing (*A51* OE) cells as determined by LC-MS analysis following methanol extraction. Results were normalized to protein content and data are represented relative to the respective wt cells as mean ± SD where n = 3.

For a) and d-e) statistical significance versus wt was evaluated by Brown-Forsythe and Welch ANOVA test in combination with Dunnett's T3 as a post hoc test.

Illustrations 5a) was generated with BioRender (https://biorender.com). mP - mitoPARP1cd, pP – pexPARP1cd, cP – cytoPARP1cd, erP – erPARP1cd.

Figure 6: The NMNAT3 equilibrium establishes a mitochondrial NAD^+ reserve in the form of NMN + ATP

a) Schematic representation of the reaction catalyzed by NMNAT3.

b) Cellular NAD^+ content in 293 *NMNAT3* knock-out (KO) and 293 *NMNAT3* overexpressing (OE) relative to 293 wt cells determined by LC-MS analysis represented as mean ± SD where n ≥ 9 biological replicates (wt: n = 21, *NMNAT3* OE cell lines: n =15, *NMNAT3* KO clone 1: n = 9, *NMNAT3* KO clone 2: n = 12).

c) Mitochondrial NAD^+ content of *NMNAT3* KO and *NMNAT3* OE cells relative to 293 wt cells determined by LC-MS analysis, represented as mean ± SD where n = 3 biological replicates.

d) PAR immunoblot analysis of lysates from parental 293 and 293 cells stably expressing mitoPARP1cd in the presence (wt) and absence (KO) of a functional *NMNAT3*.

Expression of the mitoPARP1cd fusion protein (+) was detected by its EGFP moiety, while β-tubulin and GAPDH served as loading controls.

e) Confocal fluorescence micrographs of 293 wt and *NMNAT3* KO cells stably expressing mitoPARP1cd. PAR was visualized using PAR (10H) antibody, red; DAPI staining, blue; EGFP, green; Scale bar 20 µm.

f) PAR immunoblot analysis of lysates from 293 wt, 293 *NMNAT3* KO, *SLC25A51* KO and *NMNAT3-SLC25A51* double knock-out (dKO) cells with or without stable expression of mitoPARP1cd (EGFP). GAPDH served as loading control. Results shown are representative of three repetitions.

g) Mitochondrial NMN content in *NMNAT3* KO and NMNAT3 OE relative to 293 wt cells determined by LC-MS, represented as mean ± SD where n = 3 biological replicates.

h) Magnitude of the mitochondrial NAD^+ reserve provided by NMN compared to NAD^+ itself in *NMNAT3* KO and NMNAT3 OE relative to wt 293 cells. Data are represented as mean ± SD where n = 3 biological replicates.

For b-c) and g) statistical significance was evaluated by Brown-Forsythe and Welch ANOVA test in combination with Dunnett's T3 as a post hoc test.

Figure 7: Proposed model for the cooperation of SLC25A51 and NMNAT3 to buffer cellular NAD^+ fluctuations

Under normal conditions, mitochondria take up NAD^+ from the cytosol. Part of the NAD^+ is cleaved to NMN and ATP by NMNAT3, thereby building a buffer of "NAD^+ equivalents" (left panel). When NAD^+ demand increases outside mitochondria, NAD^+ is released from the organelles through SLC25A51. Mitochondrial NAD^+ levels are

nevertheless maintained owing to the conversion of NMN and ATP back to NAD^+ by NMNAT3 (right panel).

Extended Data Figure 1: Functional validation of PARP1cd cell lines generated from 293 and HeLa S3 parental cells

a) Confocal fluorescence micrographs of HeLa S3 PARP1cd cell lines. PAR, red; DAPI staining, blue; EGFP, green. Scale bar 20 µm.

b) PAR immunoblot analysis of lysates from parental HeLa S3 (wt) and HeLa S3 PARP1cd cell lines. Samples from the same experiment were run on two different gels (PAR and GAPDH, EGFP). Results shown are representative of three repetitions.

c) PAR immunoblot analysis of lysates from parental 293 (wt) and 293 PARP1cd cell lines. Samples from the same experiment were run on two different gels (PAR and β-tubulin, EGFP and GAPDH). Results shown are representative of three repetitions.

d) Confocal fluorescence micrographs of stably transfected 293 pexPARP1cd cells. PAR, red; DAPI staining, blue; EGFP, green. Peroxisomes were detected by PMP70. Scale bar 20 µm.

e) PAR immunoblot analysis of stably transfected 293 erPARP1cd (erP) cells with and without transient overexpression of nicotinic acid phosphoribosyltransferase (NAPRT) and nicotinic acid (NA) supplementation. Expression of the erPARP1cd fusion protein was confirmed by EGFP tag, while transient overexpression of NAPRT was detected by its FLAG-tag. β-tubulin served as loading control. Results shown are representative of three independent repetitions.

f) Confocal fluorescence micrographs of stably transfected 293 erPARP1cd cells. DAPI staining, blue; EGFP, green. The ER was detected using the ER marker protein Calnexin. Scale bar 20 µm.

g) PAR immunoblot analyses of cell lysates from 293 pexPARP1cd cells (pP) incubated in the presence of 3AB (1 mM) for up to 48h. Equal sample volumes were loaded. pexPARP1cd was detected by its EGFP tag, while β-tubulin served as a loading control. Results shown are representative of four independent repetitions.

h) PAR immunoblot analyses of cell lysates from 293 pexPARP1cd cells (pP). Cells were incubated in the presence of 3AB (1 mM) for 72h. Upon washout, the cells were cultured in the absence of 3AB for up to 48h. pexPARP1cd was detected by its EGFP tag, while β-tubulin served as a loading control. Results shown are representative of four independent repetitions.

i) NAD^+/NADH ratio in PARP1cd cell lines generated from U2OS, 293 or HeLa S3 cells. Results are represented as mean ± SD where n = 9-12 biological replicates (293: n = 9; U2OS: n = 12 for wt and n = 9 for remaining conditions; HeLa S3: n = 12 for wt, remaining conditions n = 9). Statistical significance versus wt was evaluated by one-sided Brown-Forsythe and Welch ANOVA test in combination with Dunnetts T3 as a post hoc test.

Extended Data Figure 2: Metabolic and bioenergetic characterization of PARP1cd cell lines

a) Oxygen consumption rate (OCR) and extracellular acidification rate (ECAR) in 293 PARP1cd cell lines compared to parental 293 (wt) cells. Data are presented relative to 293 wt cells as mean ± SD where n = 6 for wt and n = 3 biological replicates for 293 PARP1cd cell lines.

b) Oxygen consumption rate (OCR) in stably transfected HeLa S3 PARP1cd cell lines compared to parental HeLa S3 (wt) cells. Data are presented relative to HeLa S3 wt cells as mean ± SD where n = 3 biological replicates.

c) Cell proliferation in 293 PARP1cd cell lines after 96 h incubation with galactose as the sole carbon source. Data are presented relative to cell lines grown in glucose as mean ± SD where n = 3 biological replicates.

d) Cell proliferation in HeLa S3 PARP1cd cell lines during 96 h incubation with galactose as the sole carbon source. Data are presented relative to cell lines grown in glucose as mean ± SD where n = 3 biological replicates.

e) Sensitivity towards inhibition of NamPT by FK866 (2 µM) in 293 wt cells and 293 PARP1cd cell lines in absence or presence of 3-aminobenzamide (3AB, 1 mM). Data are presented as mean ± SD where n = 3 biological replicates.

f) ATP content in PARP1cd cell lines generated from U2OS, 293 or HeLa S3 cells. Measurements were performed in presence or absence of 3AB (1 mM, 48h). Results were normalized to protein content and data are represented relative to the respective wt cells as mean ± SD where n = 9-12 biological replicates (293: n = 9; U2OS: n = 12 for wt and n = 9 for remaining conditions; HeLa S3: n = 12 for wt, remaining conditions n = 9).

g) SIRT expression levels in 293 or HeLa S3 PARP1cd cell lines relative to their parental counterparts. Gray colour indicates that changes, if any, were not significant. S

Statistical significance versus wt in Fig. S2a-d was evaluated by one-sided Brown-Forsythe and Welch ANOVA test in combination with Dunnetts T3 as a post hoc test.

Extended Data Figure 3: Isotopolog time courses for 293 PARP1cd cells and MS spectra

a) Time-dependent appearance of labeled isotopologs in stably transfected 293 PARP1cd cell lines incubated with isotope labeled nicotinamide (15N), and glucose (13C) where n = 6 biological replicates.

b) Exemplary fragment-ion spectra of NAD^+ and the NAD^+ isotopologs NAD^+ M+6 and NAD^+ M+11 as generated by MS-MS analysis from 293 cell extracts after 13.2 h of incubation with isotopically labeled nicotinamide (15N) and glucose (13C).

Extended Data Figure 4: Isotopolog time courses for wt U2OS cells and NAD^+ half-lifes in PARP1cd cell lines derived from U2OS and HeLa S3 cells

a) U2OS and HeLa S3 PARP1cd cell lines were incubated with isotopically labeled nicotinamide (18O, red) and glucose (13C, not depicted), allowing for labeling of both the Nam-moiety and the ribose-moieties.

b) The time-dependent appearance of labeled isotopologs is accompanied by the disappearance of unlabeled NAD^+ upon incubation of parental U2OS (wt) cells in the presence of isotopically labeled nicotinamide (18O), and glucose (13C) where n = 6 biological replicates.

c) Time course of label incorporation in NAD^+ in U2OS (wt) and U2OS PARP1cd cell lines. The half-life was calculated using the fitted exponential decay of the unlabeled NAD^+ and corresponds to the time point when 50% of NAD^+ is labeled (dashed line) and 50% unlabeled (solid line) where n = 6 biological replicates.

d) Time course of label incorporation in NAD^+ in HeLa S3 (wt) and HeLa S3 PARP1cd cell lines. The half-life was calculated using the fitted exponential decay of the unlabeled

NAD^+ and corresponds to the time point when 50% of NAD^+ is labeled (dashed line) and 50% unlabeled (solid line) where n = 9 biological replicates.

Extended Data Figure 5: Determination of the free mitochondrial NAD^+ using a fluorescent biosensor

a) Determination of the free mitochondrial NAD^+ concentration in HeLa cells, and upon transient transfection with mKate2-fused mitoPARP1cd (mP) and pexPARP1cd (pP) constructs using a cpVenus-based NAD^+ biosensor. NAD^+ concentrations were calculated from sensor (488/405 nm)/control (488/405 nm) fluorescence ratios determined by flow cytometry (see Extended Data Figure 5c). Data are represented relative to untransfected control cells as mean ± SD where n = 3-5 biological replicates. Statistical significance versus wt was evaluated by one-sided Brown-Forsythe and Welch ANOVA test in combination with Dunnetts T3 as a post hoc test.

b) Gating strategy for flow cytometric analysis for NAD biosensor experiments. Upon identification of the cell population (SSC-A/FSC-A), doublet exclusion was conducted (FSC-H/FSC-A). The sensor-positive cell population was identified using parental HeLa cells as a negative control (FSC-H/FITC-A). These gates were applied to HeLa NAD biosensor and cpVenus control cells. HeLa NAD biosensor cells that were not transiently transfected with red fluorescent PARP1cd constructs (MTS-mKate2-PARP1cd-myc or mKate2-PARP1cd-SKL) were used to define the PARP1cd positive (mK2+) and PARP1cd negative (mK2-) gates (FSC-H/PE-Cy5-A), which were then applied to HeLa NAD biosensor/cpVenus expressing cells transiently transfected with red fluorescent PARP1cd constructs.

c) Dose-response curve of the NAD biosensor. HeLa cells stably expressing the NAD biosensor or cpVenus control in the cytosol were permeabilized with digitonin and exposed to varying concentrations of NAD^+. The fluorescence ratio (488/405 nm) of the NAD biosensor, as measured by flow cytometry, was normalized to the fluorescence ratio (488/405 nm) of the corresponding cpVenus control and the values were plotted relative to 10 µM NAD^+. Each point represents the mean ± SD, n > 3 biological replicates.

Extended Data Figure 6: Functional and sequencing-based validation of *SLC25A51* KO clones

a) PAR immunoblot analysis of lysates from untransfected parental 293 (wt) and SLC25A51-KO cells as well as from cells one day after transient transfection with mitoPARP1cd (+). Expression of mitoPARP1cd was confirmed using GFP antibody, while β-tubulin served as loading control. Results are representative of three independent repetitions.

b) PAR immunoblot analysis of lysates from parental 293 cells as well as 293 cells and SLC25A51-KO constitutively expressing mitoPARP1cd (+). Expression of mitoPARP1cd was confirmed using GFP antibody, while β-tubulin served as loading control. Results are representative of three independent repetitions.

c) DNA Sanger sequencing analysis of the critical region targeted by the SLC25A51-specific sgRNA. Sequence chromatograms were obtained from purified RT-PCR products of the full-length open reading frames using isolated total RNA as starting material.

Extended Data Figure 7: Functional characterization of *NMNAT3* KO cell lines

a) Cellular NAD^+ content in parental HAP1 (WT) and HAP1 NMNAT3-KO cells as determined by LC-MS analysis following methanol extraction. Results were normalized to protein content and data are represented relative to the respective wt cells as mean ± SD where n = 3 biological replicates.

b) PAR immunoblot analysis of lysates from HAP1 cells transiently expressing mitoPARP1cd (+) or mitoEGFP (+) in the presence (WT) or absence (KO) of a functional NMNAT3. Expression of mitoPARP1cd and mitoEGFP was confirmed using GFP antibody, while β-tubulin served as loading control.

c) Confocal fluorescence micrographs of parental HAP1 cells and HAP1 NMNAT3-KO cells after transient transfection with mitoPARP1cd. DAPI staining, blue; EGFP (mitoPARP1cd), green; PAR, red. Scale 20 µm. d, SLC25A51 expression in parental 293 (wt) and 293 PARP1cd cell lines as well as in parental HeLa S3 (wt) and HeLa PARP1cd cell lines as determined by RNAseq. Data are represented as mean ± SD where n = 3 biological replicates. Statistical significance versus wt was evaluated by one-sided Brown-Forsythe and Welch ANOVA test in combination with Dunnetts T3 as a post hoc test. Changes were not significant.

Extended Data Figure 8: Sequencing-based validation of *NMNAT3* KO cell lines

DNA Sanger sequencing analysis of the critical region targeted by the NMNAT3-specific sgRNA in 293 cells. Sequence chromatograms were obtained from purified RT-PCR products of the full-length open reading frame using isolated total RNA as starting material.

Extended Data Figure 9: Sequencing-based validation of *NMNAT3* KO and *NMNAT3/SLC25A51* dKO cell lines

a) DNA Sanger sequencing analysis of the critical region targeted by the NMNAT3-specific sgRNA in 293 cells stably expressing mitoPARP1cd. Sequence chromatograms were obtained after RT-PCR of the full-length open reading frame using isolated total RNA as starting material.

b) DNA Sanger sequencing analysis of the critical region targeted by the SLC25A51- and NMNAT3-specific sgRNAs in 293 SLC25A51/NMNAT3 double knockout cells. Sequence chromatograms were obtained from purified RT-PCR products of the full-length open reading frames using isolated total RNA as starting material.

References

1 Canto, C., Menzies, K. J. & Auwerx, J. NAD(+) metabolism and the control of energy homeostasis: A balancing act between mitochondria and the nucleus. *Cell Metab* **22**, 31-53 (2015). https://doi.org/10.1016/j.cmet.2015.05.023

2 Katsyuba, E., Romani, M., Hofer, D. & Auwerx, J. NAD(+) homeostasis in health and disease. *Nat Metab* **2**, 9-31 (2020). https://doi.org/10.1038/s42255-019-0161-5

3 Selles Vidal, L., Kelly, C. L., Mordaka, P. M. & Heap, J. T. Review of NAD(P)H-dependent oxidoreductases: Properties, engineering and application. *Biochim Biophys Acta Proteins Proteom* **1866**, 327-347 (2018). https://doi.org/10.1016/j.bbapap.2017.11.005

4 Sultani, G., Samsudeen, A. F., Osborne, B. & Turner, N. NAD(+) : A key metabolic regulator with great therapeutic potential. *J Neuroendocrinol* **29** (2017). https://doi.org/10.1111/jne.12508

5 Yang, Y. & Sauve, A. A. NAD(+) metabolism: Bioenergetics, signaling and manipulation for therapy. *Biochim Biophys Acta* **1864**, 1787-1800 (2016). https://doi.org/10.1016/j.bbapap.2016.06.014

6 Dhuguru, J., Dellinger, R. W. & Migaud, M. E. Defining NAD(P)(H) Catabolism. *Nutrients* **15** (2023). https://doi.org/10.3390/nu15133064

7 Essuman, K. *et al.* The SARM1 toll/interleukin-1 receptor domain possesses intrinsic NAD(+) cleavage activity that promotes pathological axonal degeneration. *Neuron* **93**, 1334-1343 e1335 (2017). https://doi.org/10.1016/j.neuron.2017.02.022

8 Langelier, M. F., Eisemann, T., Riccio, A. A. & Pascal, J. M. PARP family enzymes: regulation and catalysis of the poly(ADP-ribose) posttranslational modification. *Curr Opin Struc Biol* **53**, 187-198 (2018). https://doi.org/10.1016/j.sbi.2018.11.002

9 Chini, E. N., Chini, C. C. S., Espindola Netto, J. M., de Oliveira, G. C. & van Schooten, W. The pharmacology of CD38/NADase: An emerging target in cancer and diseases of aging. *Trends Pharmacol Sci* **39**, 424-436 (2018). https://doi.org/10.1016/j.tips.2018.02.001

10 Loreto, A., Antoniou, C., Merlini, E., Gilley, J. & Coleman, M. P. NMN: The NAD precursor at the intersection between axon degeneration and anti-ageing therapies. *Neurosci Res* **197**, 18-24 (2023). https://doi.org/10.1016/j.neures.2023.01.004

11 Chini, C. C. S., Cordeiro, H. S., Tran, N. L. K. & Chini, E. N. NAD metabolism: Role in senescence regulation and aging. *Aging Cell* **23**, e13920 (2024). https://doi.org/10.1111/acel.13920

12 Wang, Y. *et al.* An overview of Sirtuins as potential therapeutic target: Structure, function and modulators. *Eur J Med Chem* **161**, 48-77 (2019). https://doi.org/10.1016/j.ejmech.2018.10.028

13 Stromland, O., Diab, J., Ferrario, E., Sverkeli, L. J. & Ziegler, M. The balance between NAD(+) biosynthesis and consumption in ageing. *Mech Ageing Dev* **199**, 111569 (2021). https://doi.org/10.1016/j.mad.2021.111569

14 Figley, M. D. *et al.* SARM1 is a metabolic sensor activated by an increased NMN/NAD(+) ratio to trigger axon degeneration. *Neuron* **109**, 1118-1136 e1111 (2021). https://doi.org/10.1016/j.neuron.2021.02.009

15 Icso, J. D., Barasa, L. & Thompson, P. R. SARM1, an Enzyme Involved in Axon Degeneration, Catalyzes Multiple Activities through a Ternary Complex Mechanism. *Biochemistry* **62**, 2065-2078 (2023). https://doi.org/10.1021/acs.biochem.3c00081

16 Guse, A. H. Enzymology of Ca(2+)-Mobilizing Second Messengers Derived from NAD: From NAD Glycohydrolases to (Dual) NADPH Oxidases. *Cells* **12** (2023). https://doi.org/10.3390/cells12040675

17 Nandave, M. *et al.* A pharmacological review on SIRT 1 and SIRT 2 proteins, activators, and inhibitors: Call for further research. *Int J Biol Macromol* **242**, 124581 (2023). https://doi.org/10.1016/j.ijbiomac.2023.124581

18 You, Y. & Liang, W. SIRT1 and SIRT6: The role in aging-related diseases. *Biochim Biophys Acta Mol Basis Dis* **1869**, 166815 (2023). https://doi.org/10.1016/j.bbadis.2023.166815

19 Kanev, P. B., Atemin, A., Stoynov, S. & Aleksandrov, R. PARP1 roles in DNA repair and DNA replication: The basi(c)s of PARP inhibitor efficacy and resistance. *Semin Oncol* **51**, 2-18 (2024). https://doi.org/10.1053/j.seminoncol.2023.08.001

20 Burgos, E. S. NAMPT in Regulated NAD Biosynthesis and its Pivotal Role in Human Metabolism. *Curr Med Chem* **18**, 1947-1961 (2011). https://doi.org/10.2174/092986711795590101

21 Burgos, E. S. & Schramm, V. L. Weak coupling of ATP hydrolysis to the chemical equilibrium of human nicotinamide phosphoribosyltransferase. *Biochemistry* **47**, 11086-11096 (2008). https://doi.org/10.1021/bi801198m

22 Khaidizar, F. D., Bessho, Y. & Nakahata, Y. Nicotinamide Phosphoribosyltransferase as a Key Molecule of the Aging/Senescence Process. *Int J Mol Sci* **22** (2021). https://doi.org/10.3390/ijms22073709

23 Imai, S. Nicotinamide Phosphoribosyltransferase (Nampt): A Link Between NAD Biology, Metabolism, and Diseases. *Curr Pharm Design* **15**, 20-28 (2009). https://doi.org/Doi 10.2174/138161209787185814

24 Preiss, J. & Handler, P. Enzymatic synthesis of nicotinamide mononucleotide. *J Biol Chem* **225**, 759-770 (1957).
25 Magni, G., Amici, A., Emanuelli, M., Raffaelli, N. & Ruggieri, S. Enzymology of NAD+ synthesis. *Adv Enzymol Relat Areas Mol Biol* **73**, 135-182, xi (1999). https://doi.org/10.1002/9780470123195.ch5
26 Berger, F., Lau, C., Dahlmann, M. & Ziegler, M. Subcellular compartmentation and differential catalytic properties of the three human nicotinamide mononucleotide adenylyltransferase isoforms. *J Biol Chem* **280**, 36334-36341 (2005). https://doi.org/10.1074/jbc.M508660200
27 Fortunato, C., Mazzola, F. & Raffaelli, N. The key role of the NAD biosynthetic enzyme nicotinamide mononucleotide adenylyltransferase in regulating cell functions. *IUBMB Life* **74**, 562-572 (2022). https://doi.org/10.1002/iub.2584
28 Preiss, J. & Handler, P. Biosynthesis of diphosphopyridine nucleotide I. Identification of intermediates. *J Biol Chem* **233**, 488-492 (1958).
29 Preiss, J. & Handler, P. Biosynthesis of diphosphopyridine nucleotide II. Enzymatic aspects. *J Biol Chem* **233**, 493-500 (1958).
30 Araki, T., Sasaki, Y. & Milbrandt, J. Increased nuclear NAD biosynthesis and SIRT1 activation prevent axonal degeneration. *Science* **305**, 1010-1013 (2004). https://doi.org/10.1126/science.1098014
31 Cambronne, X. A. & Kraus, W. L. Location, Location, Location: Compartmentalization of NAD(+) Synthesis and Functions in Mammalian Cells. *Trends Biochem Sci* **45**, 858-873 (2020). https://doi.org/10.1016/j.tibs.2020.05.010
32 Cambronne, X. A. *et al.* Biosensor reveals multiple sources for mitochondrial NAD(+). *Science* **352**, 1474-1477 (2016). https://doi.org/10.1126/science.aad5168
33 Ryu, K. W. *et al.* Metabolic regulation of transcription through compartmentalized NAD(+) biosynthesis. *Science* **360**, eaan5780 (2018). https://doi.org/10.1126/science.aan5780
34 Svoboda, P. *et al.* Nuclear transport of nicotinamide phosphoribosyltransferase is cell cycle-dependent in mammalian cells, and its inhibition slows cell growth. *J Biol Chem* **294**, 8676-8689 (2019). https://doi.org/10.1074/jbc.RA118.003505
35 Titov, D. V. *et al.* Complementation of mitochondrial electron transport chain by manipulation of the NAD(+)/NADH ratio. *Science* **352**, 231-235 (2016). https://doi.org/10.1126/science.aad4017
36 Pittelli, M. *et al.* Inhibition of nicotinamide phosphoribosyltransferase: cellular bioenergetics reveals a mitochondrial insensitive NAD pool. *J Biol Chem* **285**, 34106-34114 (2010). https://doi.org/10.1074/jbc.M110.136739
37 Yang, H. *et al.* Nutrient-sensitive mitochondrial NAD+ levels dictate cell survival. *Cell* **130**, 1095-1107 (2007). https://doi.org/10.1016/j.cell.2007.07.035
38 Hopp, A. K. *et al.* Mitochondrial NAD(+) Controls Nuclear ARTD1-Induced ADP-Ribosylation. *Mol Cell* **81**, 340-354 e345 (2021). https://doi.org/10.1016/j.molcel.2020.12.034
39 Davila, A. *et al.* Nicotinamide adenine dinucleotide is transported into mammalian mitochondria. *Elife* **7**, e33246 (2018). https://doi.org/10.7554/eLife.33246
40 Nikiforov, A., Dölle, C., Niere, M. & Ziegler, M. Pathways and subcellular compartmentation of NAD biosynthesis in human cells: from entry of extracellular precursors to mitochondrial NAD generation. *J Biol Chem* **286**, 21767-21778 (2011). https://doi.org/10.1074/jbc.M110.213298

41 Kory, N. *et al.* MCART1/SLC25A51 is required for mitochondrial NAD transport. *Sci Adv* **6**, eabe5310 (2020). https://doi.org/10.1126/sciadv.abe5310
42 Luongo, T. S. *et al.* SLC25A51 is a mammalian mitochondrial NAD+ transporter. *Nature*, 1-9 (2020). https://doi.org/0.1038/s41586-020-2741-7
43 Girardi, E. *et al.* Epistasis-driven identification of SLC25A51 as a regulator of human mitochondrial NAD import. *Nature Communications* **11** (2020). https://doi.org/10.1038/s41467-020-19871-x
44 Yamamoto, M. *et al.* Nmnat3 Is Dispensable in Mitochondrial NAD Level Maintenance In Vivo. *Plos One* **11**, e0147037 (2016). https://doi.org/10.1371/journal.pone.0147037
45 Dölle, C., Niere, M., Lohndal, E. & Ziegler, M. Visualization of subcellular NAD pools and intra-organellar protein localization by poly-ADP-ribose formation. *Cell Mol Life Sci* **67**, 433-443 (2010). https://doi.org/10.1007/s00018-009-0190-4
46 VanLinden, M. R., Niere, M., Nikiforov, A. A., Ziegler, M. & Dölle, C. Compartment-specific poly-ADP-ribose formation as a biosensor for subcellular NAD pools. *Methods Mol Biol* **1608**, 45-56 (2017). https://doi.org/10.1007/978-1-4939-6993-7_4
47 Agrimi, G., Russo, A., Scarcia, P. & Palmieri, F. The human gene SLC25A17 encodes a peroxisomal transporter of coenzyme A, FAD and NAD(+). *Biochem J* **443**, 241-247 (2012). https://doi.org/10.1042/Bj20111420
48 Khan, N. A. *et al.* Effective treatment of mitochondrial myopathy by nicotinamide riboside, a vitamin B3. *EMBO Mol Med* **6**, 721-731 (2014). https://doi.org/10.1002/emmm.201403943
49 Pirinen, E. *et al.* Niacin Cures Systemic NAD(+) Deficiency and Improves Muscle Performance in Adult-Onset Mitochondrial Myopathy. *Cell Metab* **31**, 1078-1090 e1075 (2020). https://doi.org/10.1016/j.cmet.2020.04.008
50 Bottoni, P., Gionta, G. & Scatena, R. Remarks on Mitochondrial Myopathies. *Int J Mol Sci* **24** (2022). https://doi.org/10.3390/ijms24010124
51 Chini, E. N. Of Mice and Men: NAD(+) Boosting with Niacin Provides Hope for Mitochondrial Myopathy Patients. *Cell Metab* **31**, 1041-1043 (2020). https://doi.org/10.1016/j.cmet.2020.05.013
52 Gomes, A. P. *et al.* Declining NAD(+) induces a pseudohypoxic state disrupting nuclear-mitochondrial communication during aging. *Cell* **155**, 1624-1638 (2013). https://doi.org/10.1016/j.cell.2013.11.037
53 Massudi, H. *et al.* Age-associated changes in oxidative stress and NAD+ metabolism in human tissue. *Plos One* **7**, e42357 (2012). https://doi.org/10.1371/journal.pone.0042357
54 Zhu, X.-H., Lu, M., Lee, B.-Y., Ugurbil, K. & Chen, W. In vivo NAD assay reveals the intracellular NAD contents and redox state in healthy human brain and their age dependences. *Proc Natl Acad Sci U S A* **112**, 2876-2881 (2015).
55 Covarrubias, A. J., Perrone, R., Grozio, A. & Verdin, E. NAD(+) metabolism and its roles in cellular processes during ageing. *Nat Rev Mol Cell Biol* **22**, 119-141 (2021). https://doi.org/10.1038/s41580-020-00313-x
56 Liu, L. *et al.* Quantitative analysis of NAD synthesis-breakdown fluxes. *Cell Metabolism* **27**, 1067-1087 (2018). https://doi.org/10.1016/j.cmet.2018.03.018
57 McReynolds, M. R. *et al.* NAD(+) flux is maintained in aged mice despite lower tissue concentrations. *Cell Syst* **12**, 1160-1172 e1164 (2021). https://doi.org/10.1016/j.cels.2021.09.001

58 Hasmann, M. & Schemainda, I. FK866, a highly specific noncompetitive inhibitor of nicotinamide phosphoribosyltransferase, represents a novel mechanism for induction of tumor cell apoptosis. *Cancer Res* **63**, 7436-7442 (2003).
59 Ratajczak, J. *et al.* NRK1 controls nicotinamide mononucleotide and nicotinamide riboside metabolism in mammalian cells. *Nat Commun* **7**, 13103 (2016). https://doi.org/10.1038/ncomms13103
60 Schuster, S. *et al.* FK866-induced NAMPT inhibition activates AMPK and downregulates mTOR signaling in hepatocarcinoma cells. *Biochem Biophys Res Commun* **458**, 334-340 (2015). https://doi.org/10.1016/j.bbrc.2015.01.111
61 Tan, B. *et al.* Inhibition of nicotinamide phosphoribosyltransferase (NAMPT), an enzyme essential for NAD+ biosynthesis, leads to altered carbohydrate metabolism in cancer cells. *J Biol Chem* **290**, 15812-15824 (2015). https://doi.org/10.1074/jbc.M114.632141
62 Jadeja, R. N. *et al.* Loss of NAMPT in aging retinal pigment epithelium reduces NAD(+) availability and promotes cellular senescence. *Aging (Albany NY)* **10**, 1306-1323 (2018). https://doi.org/10.18632/aging.101469
63 Shen, C. *et al.* The Depletion of NAMPT Disturbs Mitochondrial Homeostasis and Causes Neuronal Degeneration in Mouse Hippocampus. *Mol Neurobiol* **60**, 1267-1280 (2023). https://doi.org/10.1007/s12035-022-03142-5
64 Wang, W. *et al.* Decreased NAD Activates STAT3 and Integrin Pathways to Drive Epithelial-Mesenchymal Transition. *Mol Cell Proteomics* **17**, 2005-2017 (2018). https://doi.org/10.1074/mcp.RA118.000882
65 Niere, M., Kernstock, S., Koch-Nolte, F. & Ziegler, M. Functional localization of two poly(ADP-ribose)-degrading enzymes to the mitochondrial matrix. *Mol Cell Biol* **28**, 814-824 (2008). https://doi.org/10.1128/MCB.01766-07
66 VanLinden, M. R. *et al.* Subcellular distribution of NAD(+) between cytosol and mitochondria determines the metabolic profile of human cells. *J Biol Chem* **290**, 27644-27659 (2015). https://doi.org/10.1074/jbc.M115.654129
67 de Fries, R. & Mitsuhashi, M. Quantification of mitogen induced human lymphocyte proliferation: comparison of alamarBlue assay to 3H-thymidine incorporation assay. *J Clin Lab Anal* **9**, 89-95 (1995). https://doi.org/10.1002/jcla.1860090203
68 Schrader, M., Costello, J., Godinho, L. F. & Islinger, M. Peroxisome-mitochondria interplay and disease. *J Inherit Metab Dis* **38**, 681-702 (2015). https://doi.org/10.1007/s10545-015-9819-7
69 He, W., Newman, J. C., Wang, M. Z., Ho, L. & Verdin, E. Mitochondrial sirtuins: regulators of protein acylation and metabolism. *Trends Endocrinol Metab* **23**, 467-476 (2012). https://doi.org/10.1016/j.tem.2012.07.004
70 Su, X. Y., Wellen, K. E. & Rabinowitz, J. D. Metabolic control of methylation and acetylation. *Curr Opin Chem Biol* **30**, 52-60 (2016). https://doi.org/10.1016/j.cbpa.2015.10.030
71 Wellen, K. E. & Thompson, C. B. A two-way street: reciprocal regulation of metabolism and signalling. *Nat Rev Mol Cell Biol* **13**, 270-276 (2012). https://doi.org/10.1038/nrm3305
72 Sallin, O. *et al.* Semisynthetic biosensors for mapping cellular concentrations of nicotinamide adenine dinucleotides. *Elife* **7**, e32638 (2018). https://doi.org/10.7554/eLife.32638

73 Revollo, J. R., Grimm, A. A. & Imai, S. The regulation of nicotinamide adenine dinucleotide biosynthesis by Nampt/PBEF/visfatin in mammals. *Curr Opin Gastroenterol* **23**, 164-170 (2007). https://doi.org/10.1097/MOG.0b013e32801b3c8f

74 Sauter, R., Sharma, S. & Heiland, I. Accounting for NAD Concentrations in Genome-Scale Metabolic Models Captures Important Metabolic Alterations in NAD-Depleted Systems. *Biomolecules* **14**, 602 (2024). https://doi.org/10.3390/biom14050602

75 Felici, R., Lapucci, A., Ramazzotti, M. & Chiarugi, A. Insight into molecular and functional properties of NMNAT3 reveals new hints of NAD homeostasis within human mitochondria. *Plos One* **8**, e76938 (2013). https://doi.org/10.1371/journal.pone.0076938

76 Kornberg, A. The participation of inorganic pyrophosphate in the reversible enzymatic synthesis of diphosphopyridine nucleotide. *J Biol Chem* **176**, 1475 (1948).

77 Croteau, D. L., Fang, E. F., Nilsen, H. & Bohr, V. A. NAD(+) in DNA repair and mitochondrial maintenance. *Cell Cycle* **16**, 491-492 (2017). https://doi.org/10.1080/15384101.2017.1285631

78 Lee, J.-H. *et al.* Mitochondrial PARP1 regulates NAD+-dependent poly ADP-ribosylation of mitochondrial nucleoids. *Experimental & Molecular Medicine* **54**, 2135-2147 (2022). https://doi.org/10.1038/s12276-022-00894-x

79 Guldenpfennig, A. *et al.* Absence of mitochondrial SLC25A51 enhances PARP1-dependent DNA repair by increasing nuclear NAD+ levels. *Nucleic Acids Res* **51**, 9248-9265 (2023). https://doi.org/10.1093/nar/gkad659

80 Canto, C. NAD(+) Precursors: A Questionable Redundancy. *Metabolites* **12** (2022). https://doi.org/10.3390/metabo12070630

81 Guarente, L., Sinclair, D. A. & Kroemer, G. Human trials exploring anti-aging medicines. *Cell Metab* **36**, 354-376 (2024). https://doi.org/10.1016/j.cmet.2023.12.007

82 She, J., Sheng, R. & Qin, Z. H. Pharmacology and Potential Implications of Nicotinamide Adenine Dinucleotide Precursors. *Aging Dis* **12**, 1879-1897 (2021). https://doi.org/10.14336/ad.2021.0523

83 Yoshino, J., Baur, J. A. & Imai, S.-i. NAD+ Intermediates: The Biology and Therapeutic Potential of NMN and NR. *Cell Metabolism* **27**, 513-528 (2018). https://doi.org/https://doi.org/10.1016/j.cmet.2017.11.002

84 Damgaard, M. V. & Treebak, J. T. What is really known about the effects of nicotinamide riboside supplementation in humans. *Sci Adv* **9**, eadi4862 (2023). https://doi.org/10.1126/sciadv.adi4862

85 Lautrup, S., Hou, Y., Fang, E. F. & Bohr, V. A. Roles of NAD(+) in Health and Aging. *Cold Spring Harb Perspect Med* **14** (2024). https://doi.org/10.1101/cshperspect.a041193

86 Song, Q. *et al.* The Safety and Antiaging Effects of Nicotinamide Mononucleotide in Human Clinical Trials: an Update. *Adv Nutr* **14**, 1416-1435 (2023). https://doi.org/10.1016/j.advnut.2023.08.008

87 Bieganowski, P. & Brenner, C. Discoveries of nicotinamide riboside as a nutrient and conserved NRK genes establish a Preiss-Handler independent route to NAD+ in fungi and humans. *Cell* **117**, 495-502 (2004). https://doi.org/10.1016/s0092-8674(04)00416-7

88 Migaud, M. E., Ziegler, M. & Baur, J. A. Regulation of and challenges in targeting NAD(+) metabolism. *Nat Rev Mol Cell Biol* **25**, 822-840 (2024). https://doi.org/10.1038/s41580-024-00752-w

89 Lu, M.-J. *et al.* SLC25A51 decouples the mitochondrial NAD+/NADH ratio to control proliferation of AML cells. *Cell Metabolism* **36**, 808-821.e806 (2024). https://doi.org/https://doi.org/10.1016/j.cmet.2024.01.013

90 Hikosaka, K. *et al.* Deficiency of nicotinamide mononucleotide adenylyltransferase 3 (nmnat3) causes hemolytic anemia by altering the glycolytic flow in mature erythrocytes. *J Biol Chem* **289**, 14796-14811 (2014). https://doi.org/10.1074/jbc.M114.554378

91 Di Lisa, F. & Ziegler, M. Pathophysiological relevance of mitochondria in NAD(+) metabolism. *FEBS Lett* **492**, 4-8 (2001). https://doi.org/10.1016/s0014-5793(01)02198-6

92 Sallin, O. *et al.* Semisynthetic biosensors for mapping cellular concentrations of nicotinamide adenine dinucleotides. *Elife* **7** (2018). https://doi.org/10.7554/eLife.32638

93 Griffiths, E. J. & Halestrap, A. P. Pyrophosphate metabolism in the perfused heart and isolated heart mitochondria and its role in regulation of mitochondrial function by calcium. *Biochemical Journal* **290**, 489-495 (1993). https://doi.org/10.1042/bj2900489

94 Sorci, L. *et al.* Initial-rate kinetics of human NMN-adenylyltransferases: substrate and metal ion specificity, inhibition by products and multisubstrate analogues, and isozyme contributions to NAD+ biosynthesis. *Biochemistry* **46**, 4912-4922 (2007). https://doi.org/10.1021/bi6023379

95 Ran, F. A. *et al.* Genome engineering using the CRISPR-Cas9 system. *Nat Protoc* **8**, 2281-2308 (2013). https://doi.org/10.1038/nprot.2013.143

96 Love, M. I., Huber, W. & Anders, S. Moderated estimation of fold change and dispersion for RNA-seq data with DESeq2. *Genome Biology* **15**, 550 (2014). https://doi.org/10.1186/s13059-014-0550-8

97 Virtanen, P. *et al.* SciPy 1.0: fundamental algorithms for scientific computing in Python. *Nature Methods* **17**, 261-272 (2020). https://doi.org/10.1038/s41592-019-0686-2

98 Meier, S., Mjos, S. A., Joensen, H. & Grahl-Nielsen, O. Validation of a one-step extraction/methylation method for determination of fatty acids and cholesterol in marine tissues. *J Chromatogr A* **1104**, 291-298 (2006). https://doi.org/10.1016/j.chroma.2005.11.045

99 Mjos, S. A. Identification of fatty acids in gas chromatography by application of different temperature and pressure programs on a single capillary column. *J Chromatogr A* **1015**, 151-161 (2003). https://doi.org/10.1016/s0021-9673(03)01240-8

100 Sciotto, C. & Mjos, S. A. Trans isomers of EPA and DHA in omega-3 products on the European market. *Lipids* **47**, 659-667 (2012). https://doi.org/10.1007/s11745-012-3672-3

101 Giskeodegard, G. F. *et al.* Metabolic markers in blood can separate prostate cancer from benign prostatic hyperplasia. *Br J Cancer* **113**, 1712-1719 (2015). https://doi.org/10.1038/bjc.2015.411

102 Makarov, M. V., Harris, N. W., Rodrigues, M. & Migaud, M. E. Scalable syntheses of traceable ribosylated NAD(+) precursors. *Org Biomol Chem* **17**, 8716-8720 (2019). https://doi.org/10.1039/c9ob01981b

103 Shchepin, R. V., Barskiy, D. A., Mikhaylov, D. M. & Chekmenev, E. Y. Efficient Synthesis of Nicotinamide-1-15N for Ultrafast NMR Hyperpolarization Using Parahydrogen. *Bioconjugate Chemistry* **27**, 878-882 (2016). https://doi.org/10.1021/acs.bioconjchem.6b00148

104 Houry, D. *et al.* Identification of structural determinants of nicotinamide phosphoribosyl transferase (NAMPT) activity and substrate selectivity. *J Struct Biol* **215**, 108004 (2023). https://doi.org/10.1016/j.jsb.2023.108004

105 Dietze, J. *et al.* Natural isotope correction improves analysis of protein modification dynamics. *Analytical and Bioanalytical Chemistry* **413** (2021). https://doi.org/10.1007/s00216-021-03732-7

106 Schäuble, S., Stavrum, A. K., Puntervoll, P., Schuster, S. & Heiland, I. Effect of substrate competition in kinetic models of metabolic networks. *FEBS Letters* **587**, 2818-2824 (2013). https://doi.org/10.1016/j.febslet.2013.06.025

107 Hoops, S. *et al.* COPASI--a COmplex PAthway SImulator. *Bioinformatics* **22**, 3067-3074 (2006). https://doi.org/10.1093/bioinformatics/btl485

108 Fisher, R. A. in *Breakthroughs in Statistics: Methodology and Distribution* (eds Samuel Kotz & Norman L. Johnson) 66-70 (Springer New York, 1992).

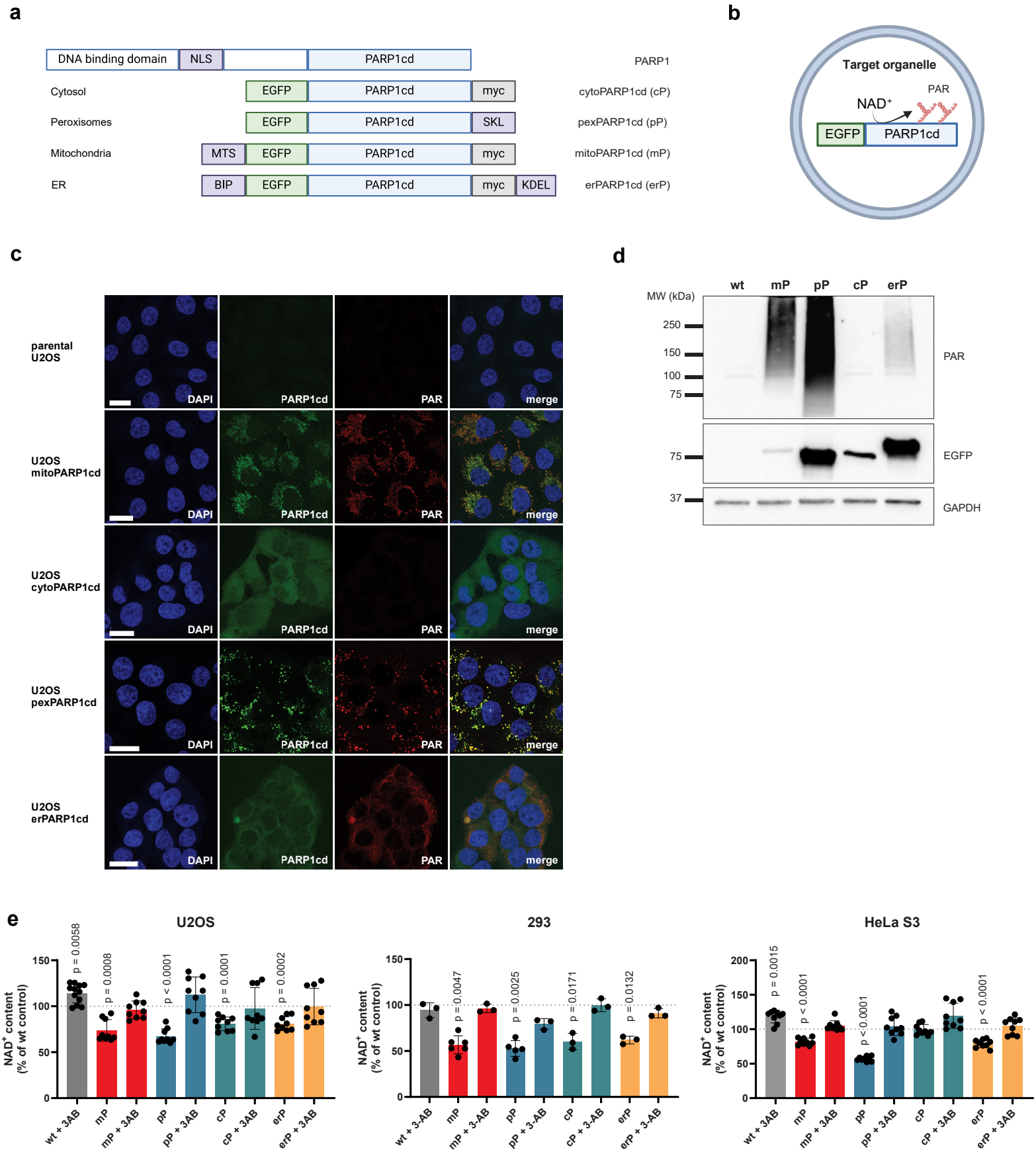
a
DNA binding domain
NLS
PARP1cd
PARP1
Cytosol
EGFP
PARP1cd
myc
cytoPARP1cd (cP)
Peroxisomes
EGFP
PARP1cd
SKL
pexPARP1cd (pP)
Mitochondria
MTS
EGFP
PARP1cd
myc
mitoPARP1cd (mP)
ER
BIP
EGFP
PARP1cd
myc
KDEL
erPARP1cd (erP)
b
Target organelle
PAR
NAD+
EGFP
PARP1cd
c
parental U2OS
U2OS mitoPARP1cd
U2OS cytoPARP1cd
U2OS pexPARP1cd
U2OS erPARP1cd
DAPI
PARP1cd
PAR
merge
d
wt
mP
pP
cP
erP
MW (kDa)
250
150
100
75
PAR
75
EGFP
37
GAPDH
e
U2OS
293
HeLa S3
NAD+ content (% of wt control)
p = 0.0058
p = 0.0008
p < 0.0001
p = 0.0001
p = 0.0002
p = 0.0047
p = 0.0025
p = 0.0171
p = 0.0132
p = 0.0015
p < 0.0001
p < 0.0001
p < 0.0001
wt + 3AB
mP
mP + 3AB
pP
pP + 3AB
cP
cP + 3AB
erP
erP + 3AB

Figure 1

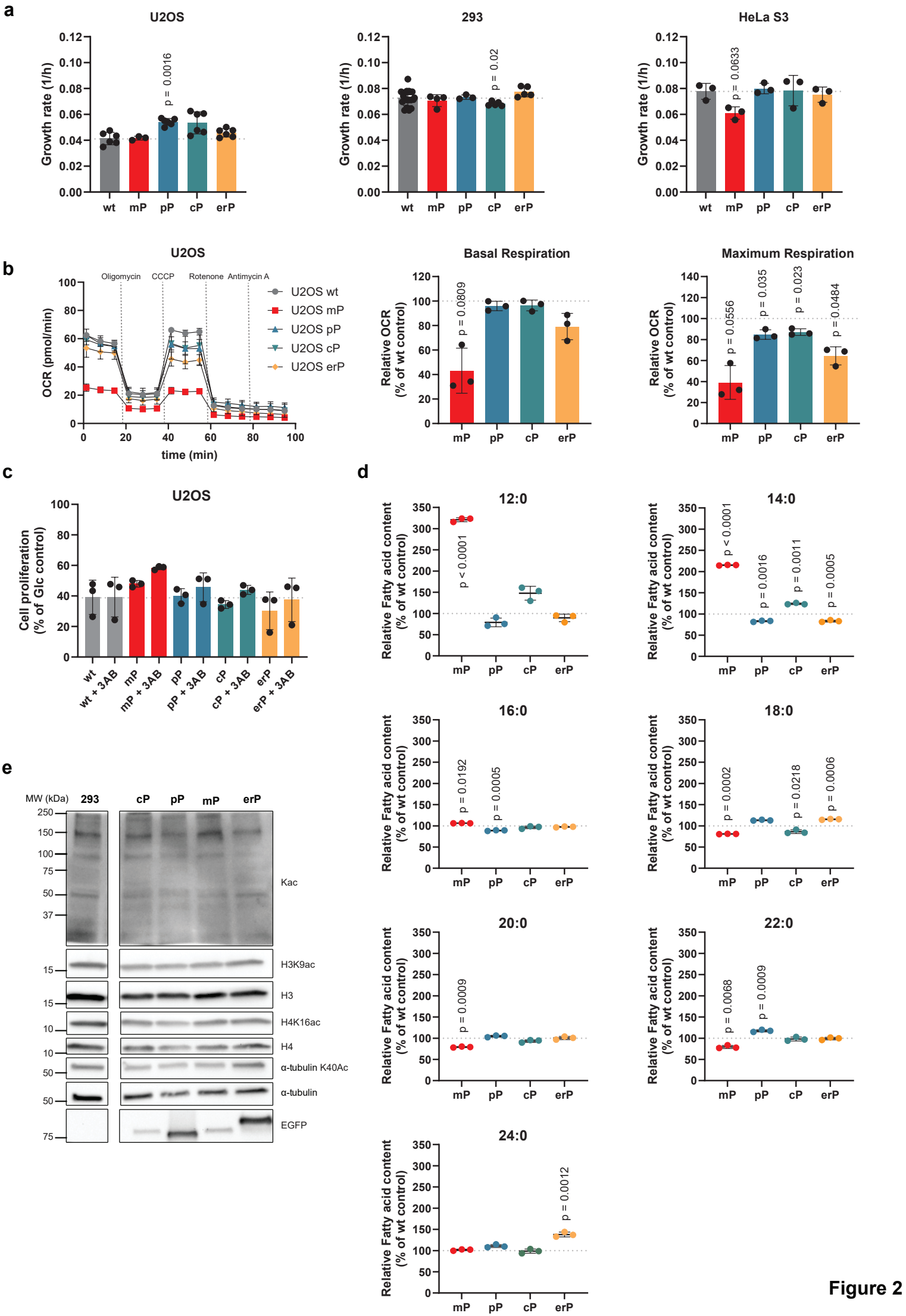
a
U2OS
293
HeLa S3
Growth rate (1/h)
p = 0.0016
p = 0.02
p = 0.0633
wt
mP
pP
cP
erP
b
U2OS
Oligomycin
CCCP
Rotenone
Antimycin A
U2OS wt
U2OS mP
U2OS pP
U2OS cP
U2OS erP
OCR (pmol/min)
time (min)
Basal Respiration
Maximum Respiration
Relative OCR (% of wt control)
p = 0.0809
p = 0.0556
p = 0.035
p = 0.023
p = 0.0484
c
U2OS
Cell proliferation (% of Glc control)
wt
wt + 3AB
mP
mP + 3AB
pP
pP + 3AB
cP
cP + 3AB
erP
erP + 3AB
d
12:0
14:0
16:0
18:0
20:0
22:0
24:0
Relative Fatty acid content (% of wt control)
p < 0.0001
p = 0.0016
p = 0.0011
p = 0.0005
p = 0.0192
p = 0.0002
p = 0.0218
p = 0.0006
p = 0.0009
p = 0.0068
p = 0.0012
e
MW (kDa)
293
cP
pP
mP
erP
Kac
H3K9ac
H3
H4K16ac
H4
α-tubulin K40Ac
α-tubulin
EGFP

Figure 2

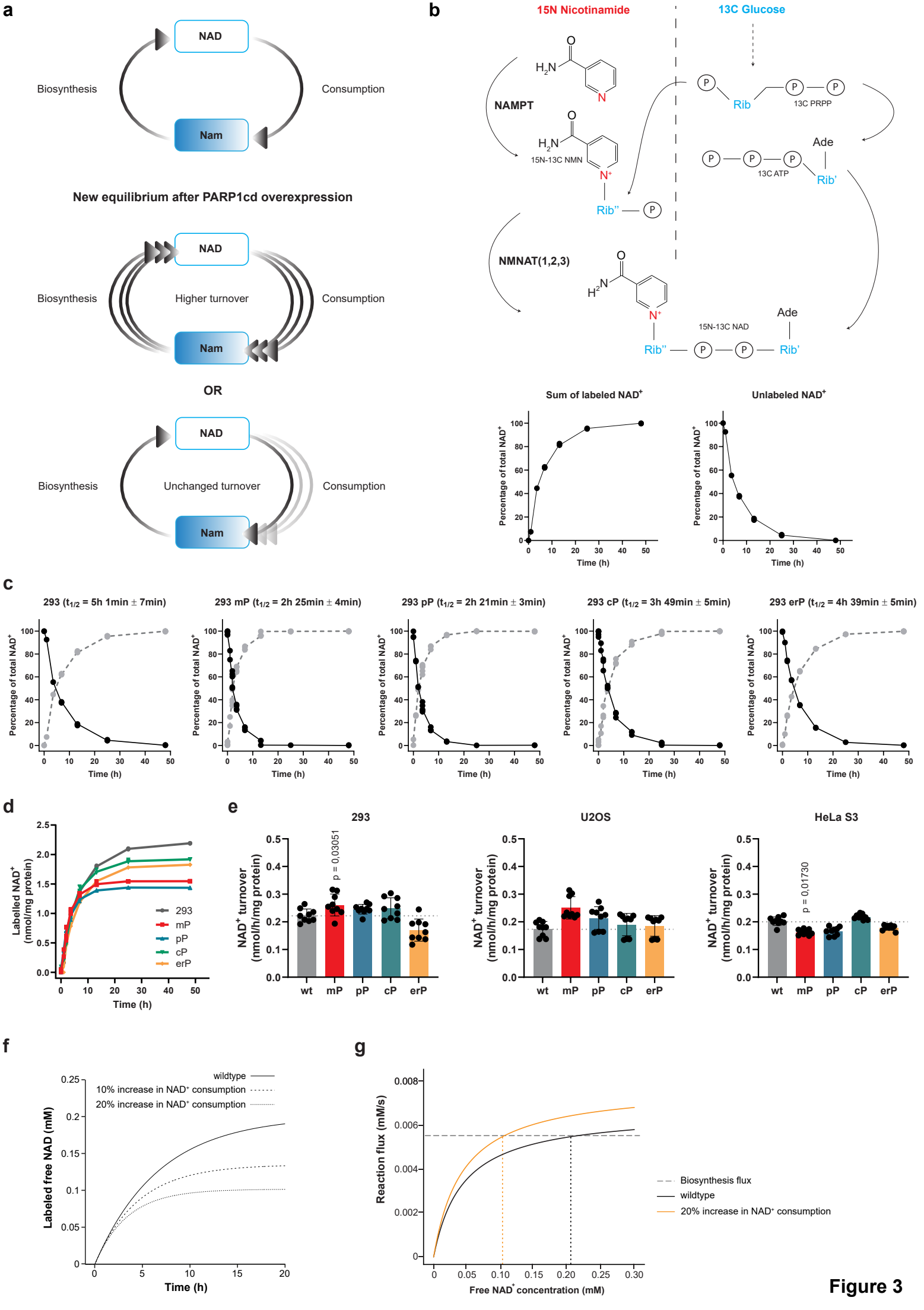
a
NAD
Biosynthesis
Consumption
Nam
New equilibrium after PARP1cd overexpression
NAD
Biosynthesis
Higher turnover
Consumption
Nam
OR
NAD
Biosynthesis
Unchanged turnover
Consumption
Nam
b
15N Nicotinamide
13C Glucose
NAMPT
15N-13C NMN
Rib
13C PRPP
Ade
13C ATP
Rib'
Rib''
NMNAT(1,2,3)
15N-13C NAD
Sum of labeled NAD+
Unlabeled NAD+
Percentage of total NAD+
Time (h)
c
293 (t1/2 = 5h 1min ± 7min)
293 mP (t1/2 = 2h 25min ± 4min)
293 pP (t1/2 = 2h 21min ± 3min)
293 cP (t1/2 = 3h 49min ± 5min)
293 erP (t1/2 = 4h 39min ± 5min)
Percentage of total NAD+
Time (h)
d
Labelled NAD+ (nmol/mg protein)
293
mP
pP
cP
erP
Time (h)
e
293
U2OS
HeLa S3
NAD+ turnover (nmol/h/mg protein)
p = 0,03051
p = 0,01730
wt
mP
pP
cP
erP
f
wildtype
10% increase in NAD+ consumption
20% increase in NAD+ consumption
Labeled free NAD (mM)
Time (h)
g
Reaction flux (mM/s)
Biosynthesis flux
wildtype
20% increase in NAD+ consumption
Free NAD+ concentration (mM)

Figure 3

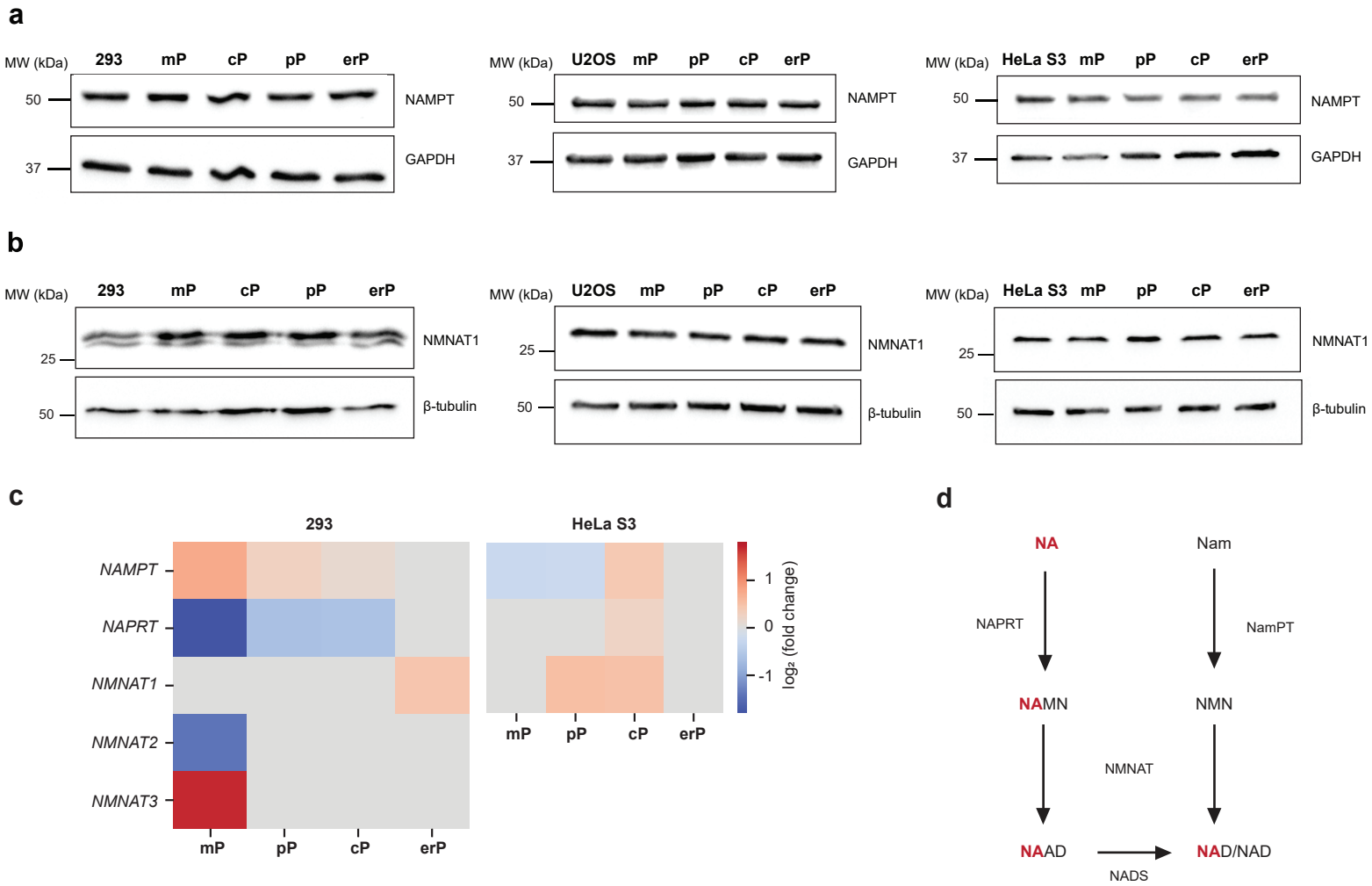
a
MW (kDa)
293
mP
cP
pP
erP
50
37
NAMPT
GAPDH
U2OS
HeLa S3
b
25
NMNAT1
β-tubulin
c
293
HeLa S3
NAMPT
NAPRT
NMNAT1
NMNAT2
NMNAT3
log₂ (fold change)
d
NA
Nam
NAPRT
NamPT
NAMN
NMN
NMNAT
NAAD
NAD/NAD
NADS
e
Total NAD⁺ (%)
p = 0.0007
NAD⁺ ¹³C
NAD⁺ ¹²C
wt
f
p < 0.0001
p = 0.0013
p = 0.0008
p = 0.0259

Figure 4

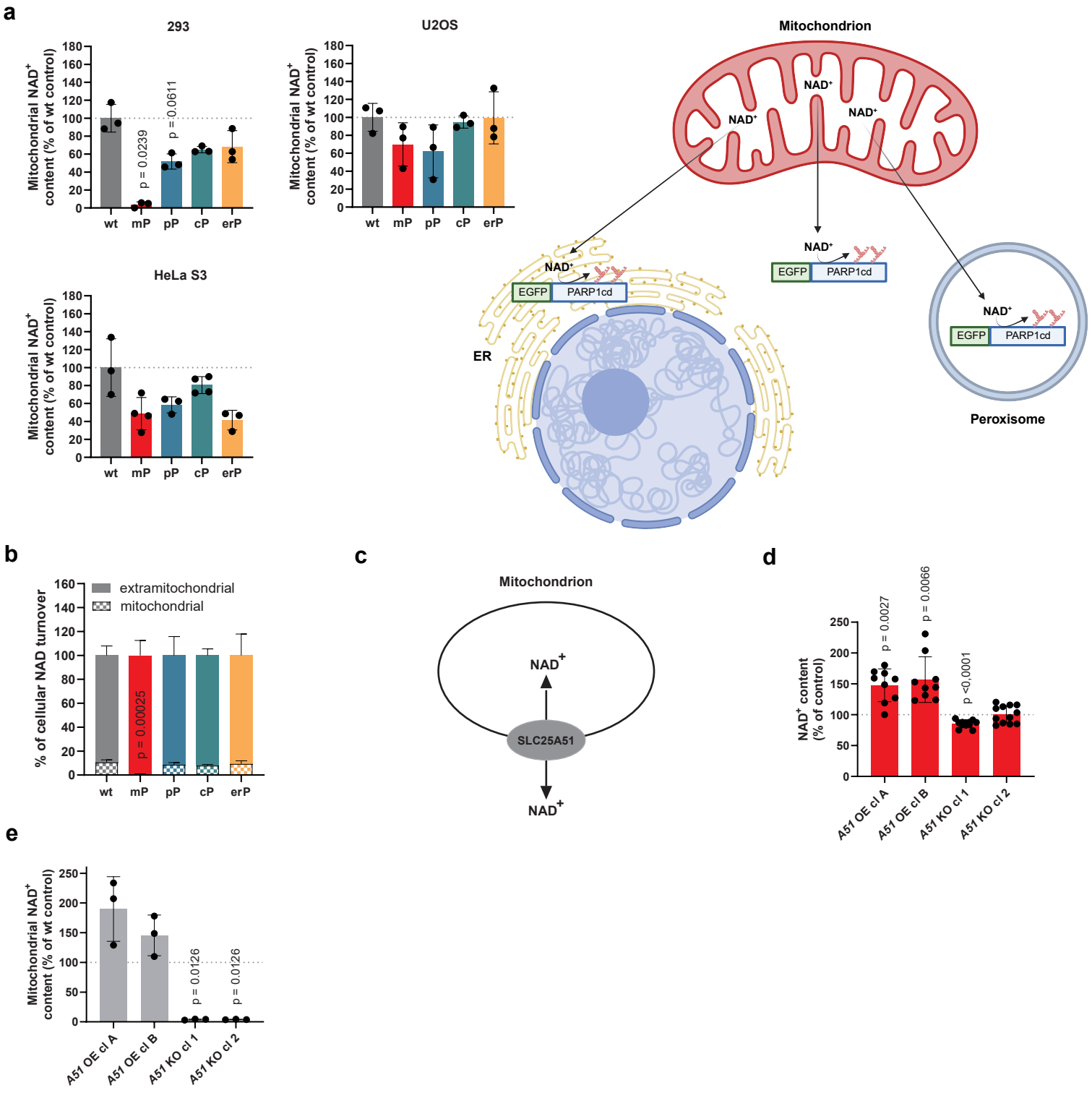
a
293
U2OS
HeLa S3
Mitochondrial NAD+ content (% of wt control)
wt
mP
pP
cP
erP
p = 0.0239
p = 0.0611
Mitochondrion
NAD+
EGFP
PARP1cd
ER
Peroxisome
b
% of cellular NAD turnover
extramitochondrial
mitochondrial
p = 0.00025
c
Mitochondrion
SLC25A51
d
NAD+ content (% of control)
p = 0.0027
p = 0.0066
p <0.0001
A51 OE cl A
A51 OE cl B
A51 KO cl 1
A51 KO cl 2
e
p = 0.0126
p = 0.0126

Figure 5

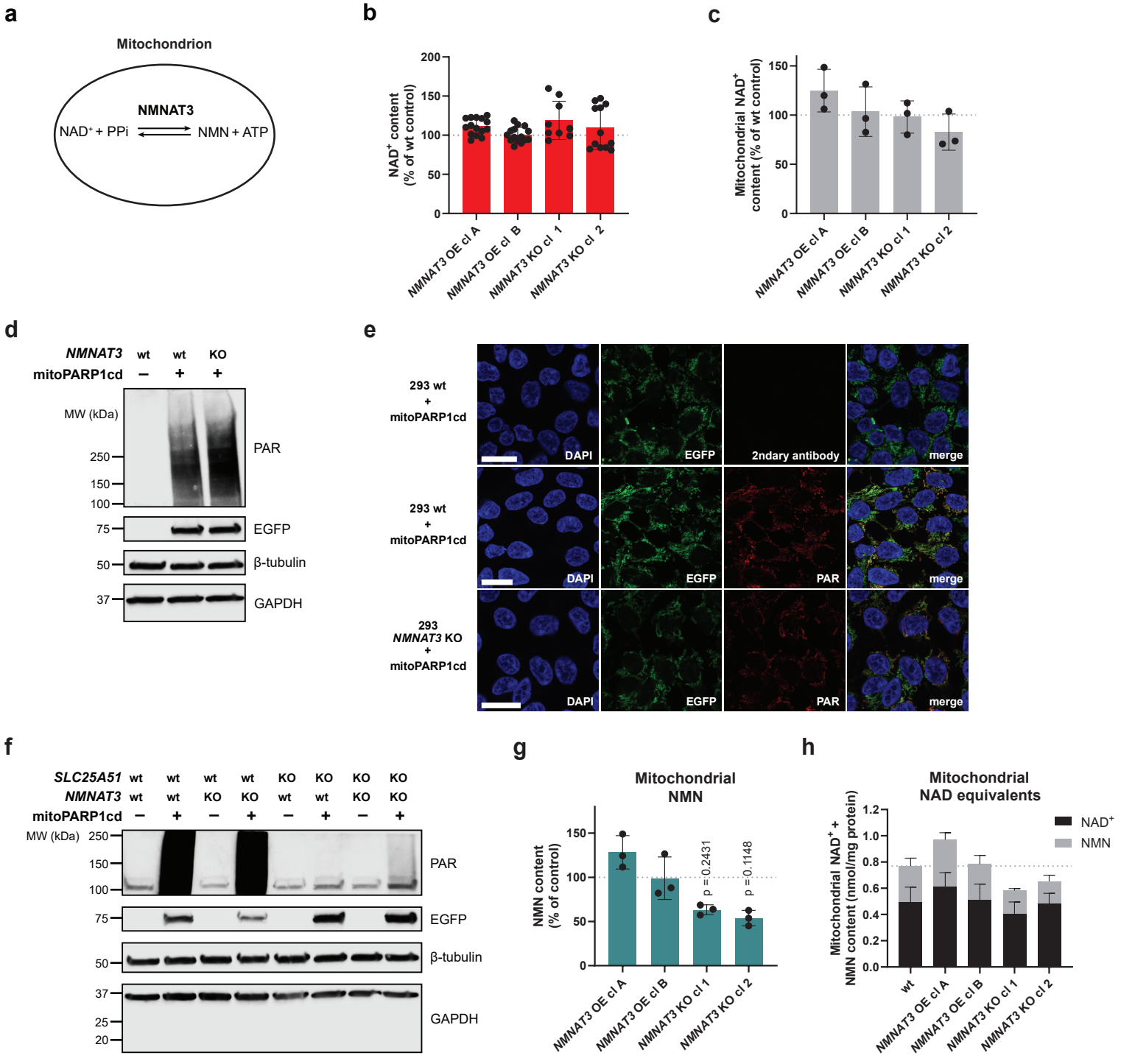
a
Mitochondrion
NMNAT3
NAD+ + PPi
NMN + ATP
b
NAD+ content (% of wt control)
NMNAT3 OE cl A
NMNAT3 OE cl B
NMNAT3 KO cl 1
NMNAT3 KO cl 2
c
Mitochondrial NAD+ content (% of wt control)
d
NMNAT3 wt wt KO
mitoPARP1cd – + +
MW (kDa)
PAR
EGFP
β-tubulin
GAPDH
e
293 wt + mitoPARP1cd
293 NMNAT3 KO + mitoPARP1cd
DAPI
EGFP
2ndary antibody
PAR
merge
f
SLC25A51
NMNAT3
mitoPARP1cd
g
Mitochondrial NMN
NMN content (% of control)
p = 0.2431
p = 0.1148
h
Mitochondrial NAD equivalents
Mitochondrial NAD+ + NMN content (nmol/mg protein)
NAD+
NMN
wt

Figure 6

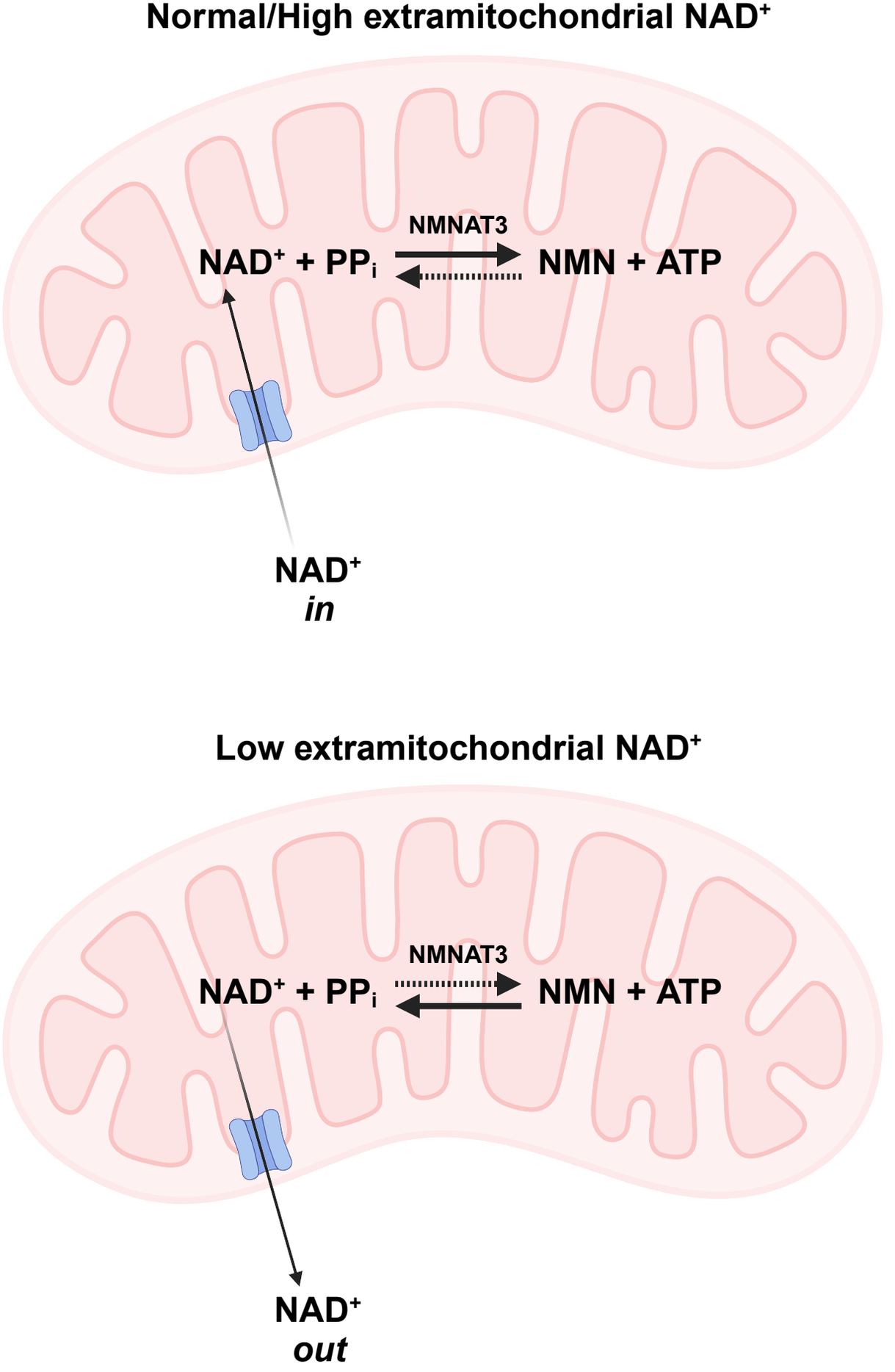
Normal/High extramitochondrial NAD+
NMNAT3
NAD+ + PPi
NMN + ATP
NAD+
in
Low extramitochondrial NAD+
NMNAT3
NAD+ + PPi
NMN + ATP
NAD+
out

Figure 7

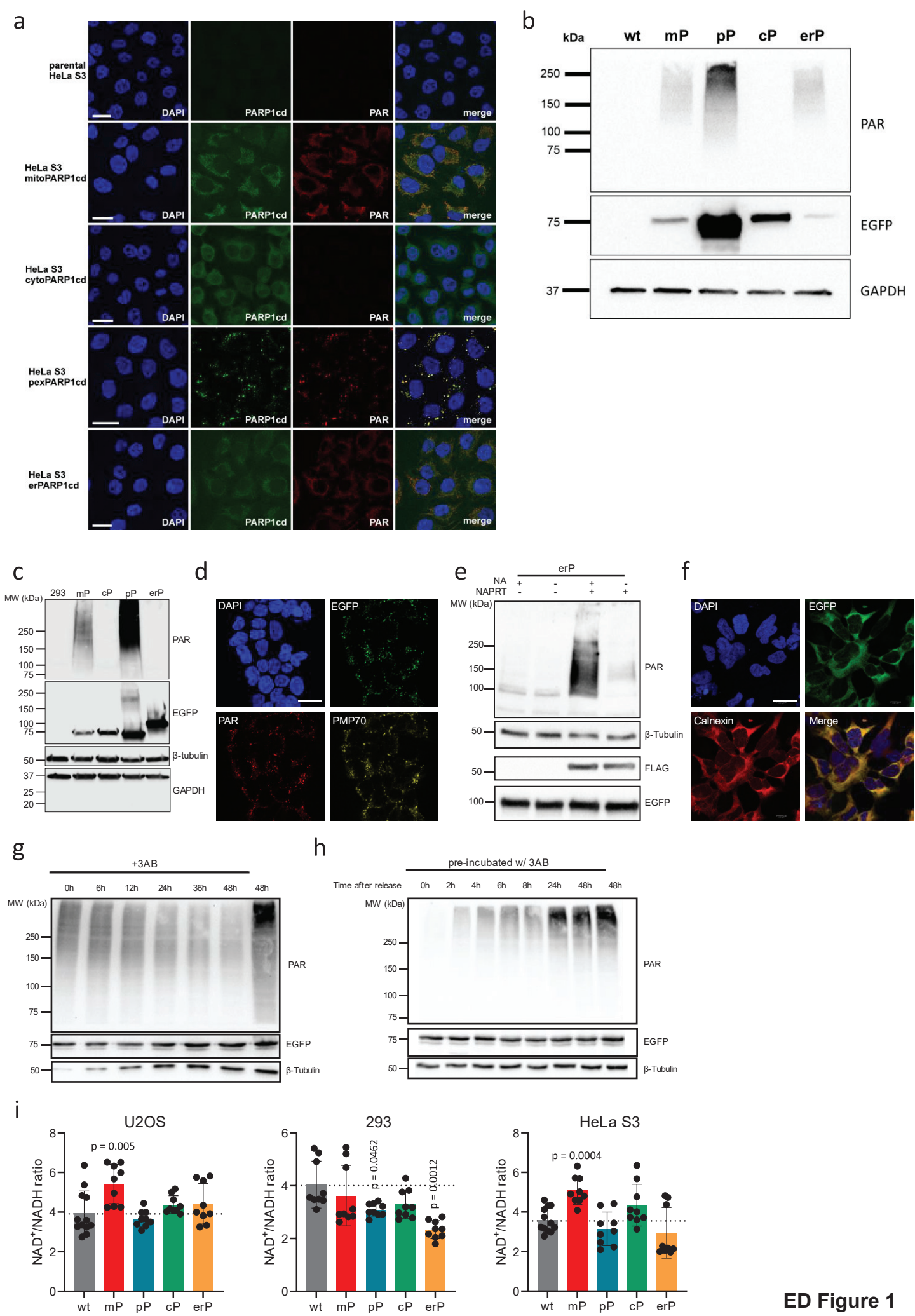
a
parental HeLa S3
HeLa S3 mitoPARP1cd
HeLa S3 cytoPARP1cd
HeLa S3 pexPARP1cd
HeLa S3 erPARP1cd
DAPI
PARP1cd
PAR
merge
b
kDa
wt
mP
pP
cP
erP
250
150
100
75
37
PAR
EGFP
GAPDH
c
293
mP
cP
pP
erP
MW (kDa)
250
150
100
75
50
37
25
20
PAR
EGFP
β-tubulin
GAPDH
d
DAPI
EGFP
PAR
PMP70
e
erP
NA
NAPRT
MW (kDa)
250
150
100
50
PAR
β-Tubulin
FLAG
EGFP
f
DAPI
EGFP
Calnexin
Merge
g
+3AB
0h
6h
12h
24h
36h
48h
48h
MW (kDa)
250
150
100
75
50
PAR
EGFP
β-Tubulin
h
pre-incubated w/ 3AB
Time after release
0h
2h
4h
6h
8h
24h
48h
48h
MW (kDa)
250
150
100
75
50
PAR
EGFP
β-Tubulin
i
U2OS
293
HeLa S3
NAD+/NADH ratio
p = 0.005
p = 0.0462
p = 0.0012
p = 0.0004
wt
mP
pP
cP
erP

ED Figure 1

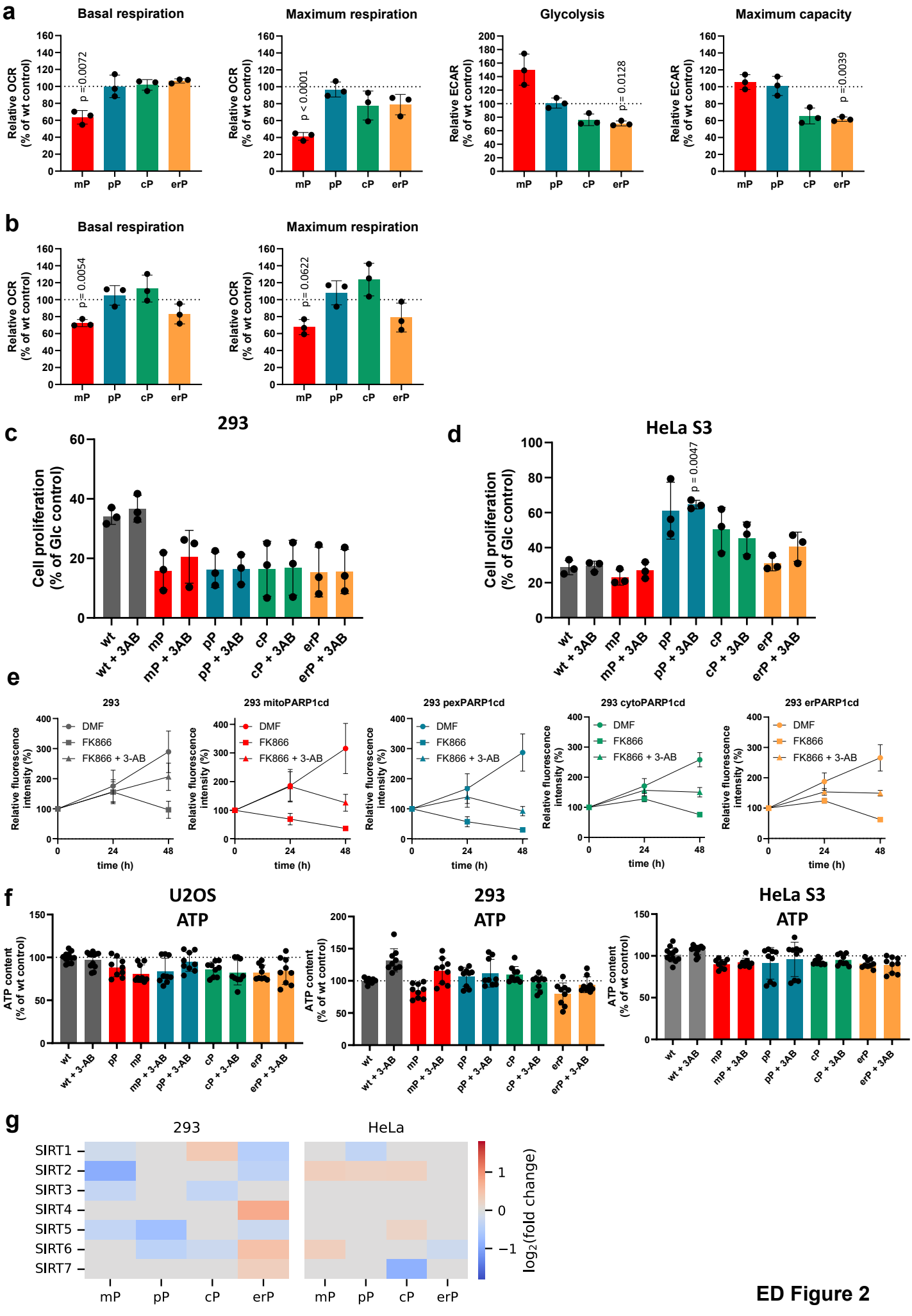
a
Basal respiration
Maximum respiration
Glycolysis
Maximum capacity
Relative OCR (% of wt control)
Relative ECAR (% of wt control)
p =0.0072
p < 0.0001
p= 0.0128
p =0.0039
mP
pP
cP
erP
b
Basal respiration
Maximum respiration
p= 0.0054
p= 0.0622
c
293
Cell proliferation (% of Glc control)
wt
wt + 3AB
mP
mP + 3AB
pP
pP + 3AB
cP
cP + 3AB
erP
erP + 3AB
d
HeLa S3
p = 0.0047
e
293
293 mitoPARP1cd
293 pexPARP1cd
293 cytoPARP1cd
293 erPARP1cd
DMF
FK866
FK866 + 3-AB
Relative fluorescence intensity (%)
time (h)
f
U2OS
ATP
293
ATP
HeLa S3
ATP
ATP content (% of wt control)
g
293
HeLa
SIRT1
SIRT2
SIRT3
SIRT4
SIRT5
SIRT6
SIRT7
log2(fold change)

ED Figure 2

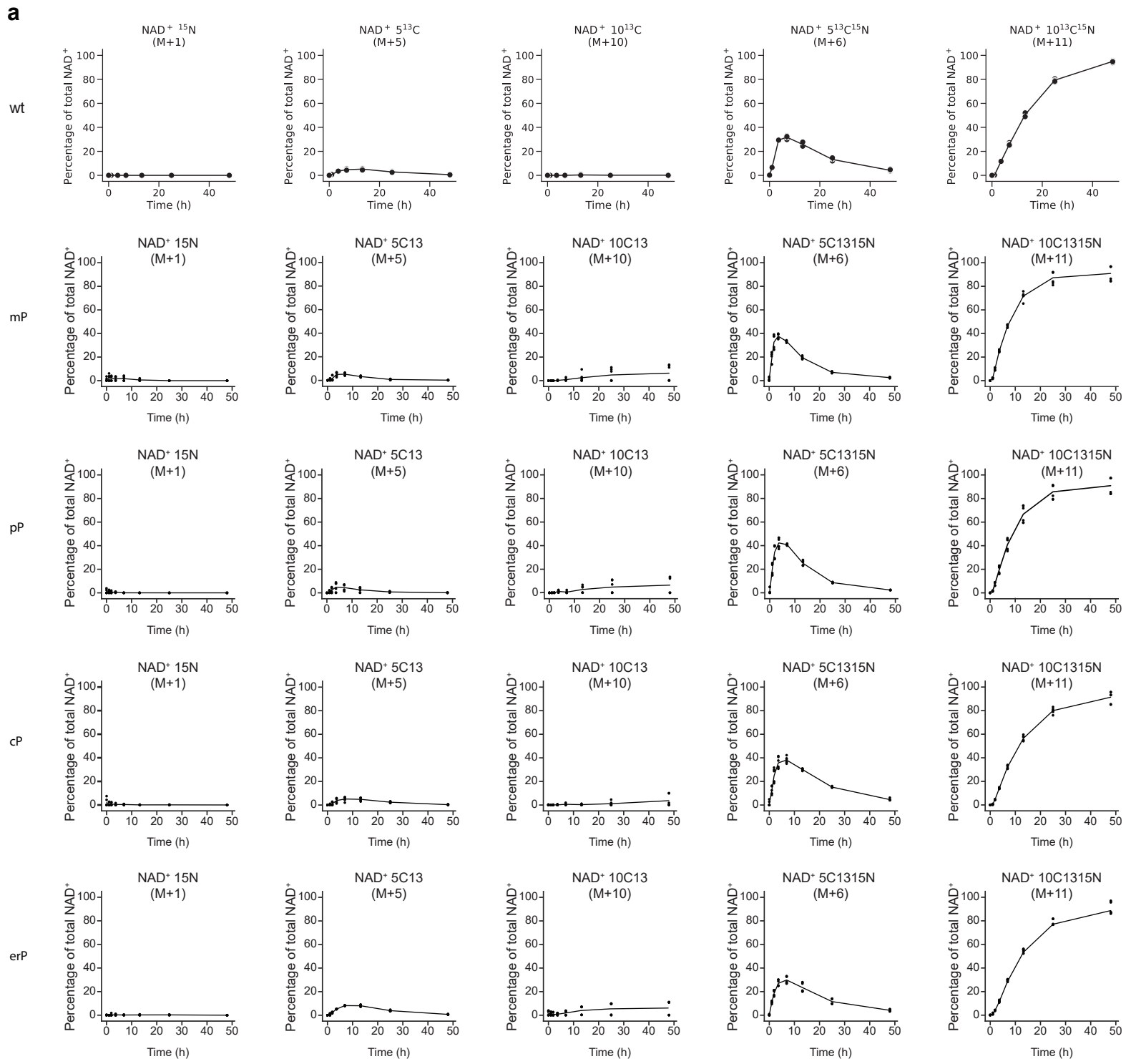
a
wt
mP
pP
cP
erP
NAD+ 15N (M+1)
NAD+ 5C13 (M+5)
NAD+ 10C13 (M+10)
NAD+ 5C1315N (M+6)
NAD+ 10C1315N (M+11)
Percentage of total NAD+
Time (h)

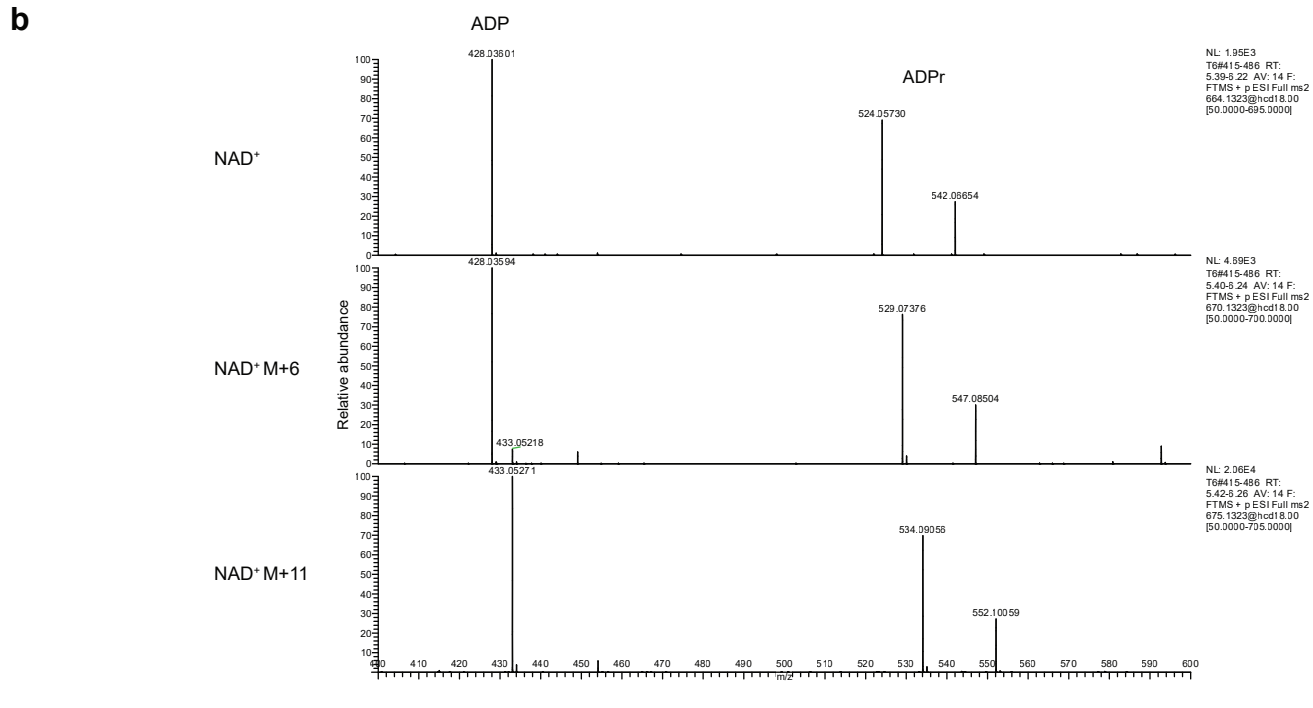
b
ADP
ADPr
NAD+
NAD+M+6
NAD+M+11
Relative abundance
m/z
428.03601
524.05730
542.06654
428.03594
529.07376
547.08504
433.05218
433.05271
534.09056
552.10059

ED Figure 3

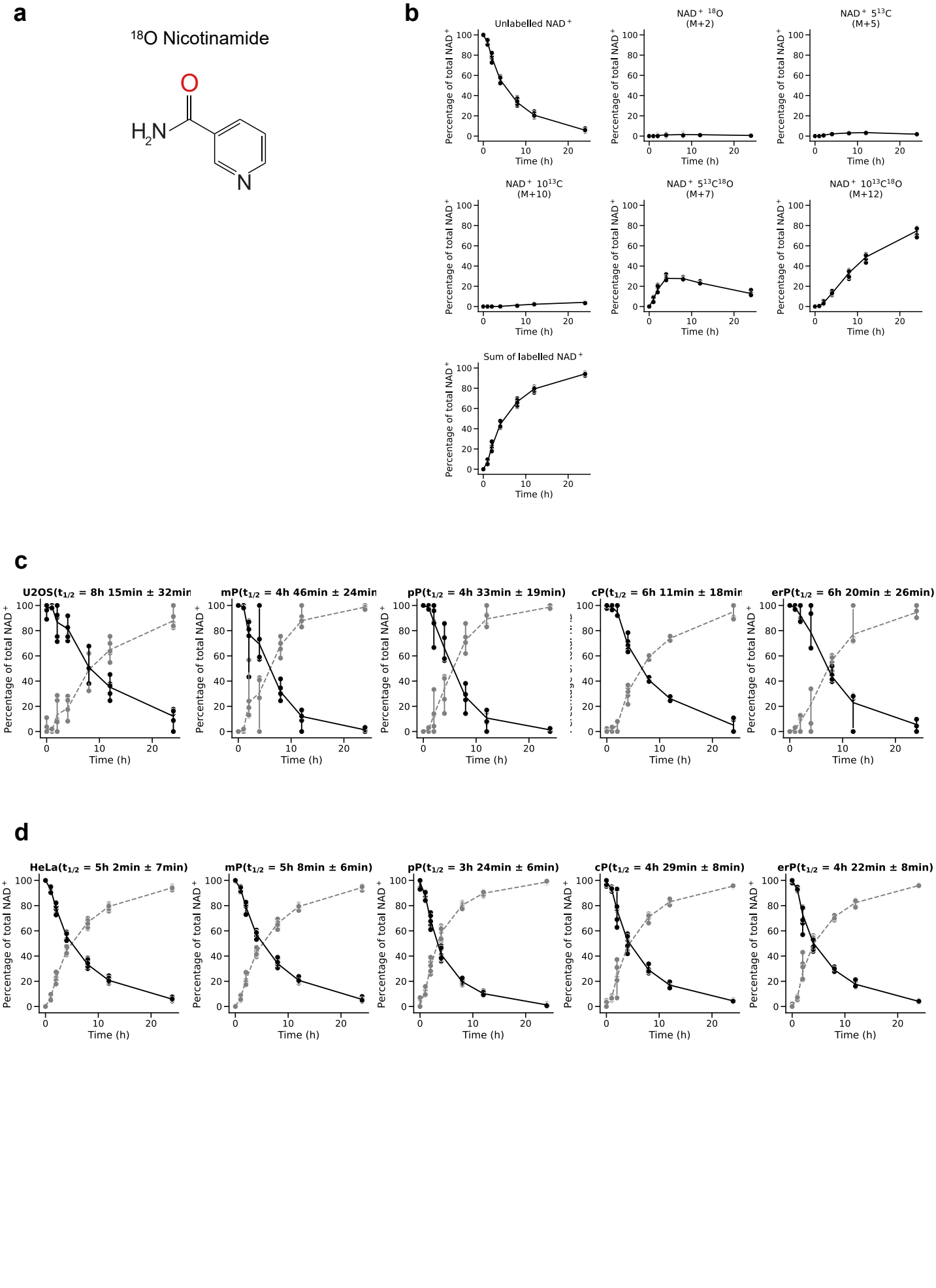
a
^{18}O Nicotinamide
O
H_2N
N
b
Unlabelled NAD$^+$
NAD$^+$ ^{18}O (M+2)
NAD$^+$ ^{13}C (M+5)
NAD$^+$ ^{10}^{13}C (M+10)
NAD$^+$ ^{5}^{13}C^{18}O (M+7)
NAD$^+$ ^{10}^{13}C^{18}O (M+12)
Sum of labelled NAD$^+$
Percentage of total NAD$^+$
Time (h)
c
U2OS($t_{1/2}$ = 8h 15min ± 32min
mP($t_{1/2}$ = 4h 46min ± 24min
pP($t_{1/2}$ = 4h 33min ± 19min)
cP($t_{1/2}$ = 6h 11min ± 18min
erP($t_{1/2}$ = 6h 20min ± 26min)
d
HeLa($t_{1/2}$ = 5h 2min ± 7min)
mP($t_{1/2}$ = 5h 8min ± 6min)
pP($t_{1/2}$ = 3h 24min ± 6min)
cP($t_{1/2}$ = 4h 29min ± 8min)
erP($t_{1/2}$ = 4h 22min ± 8min)

ED Figure 4

a

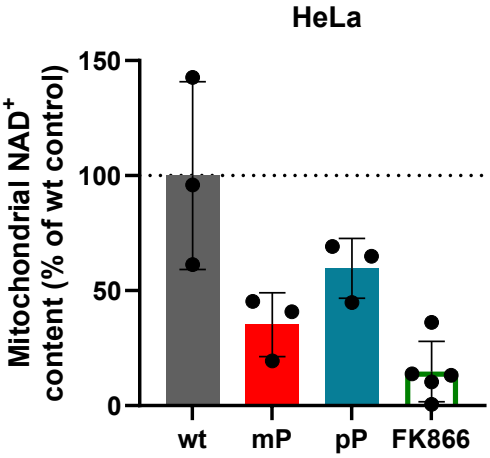

b

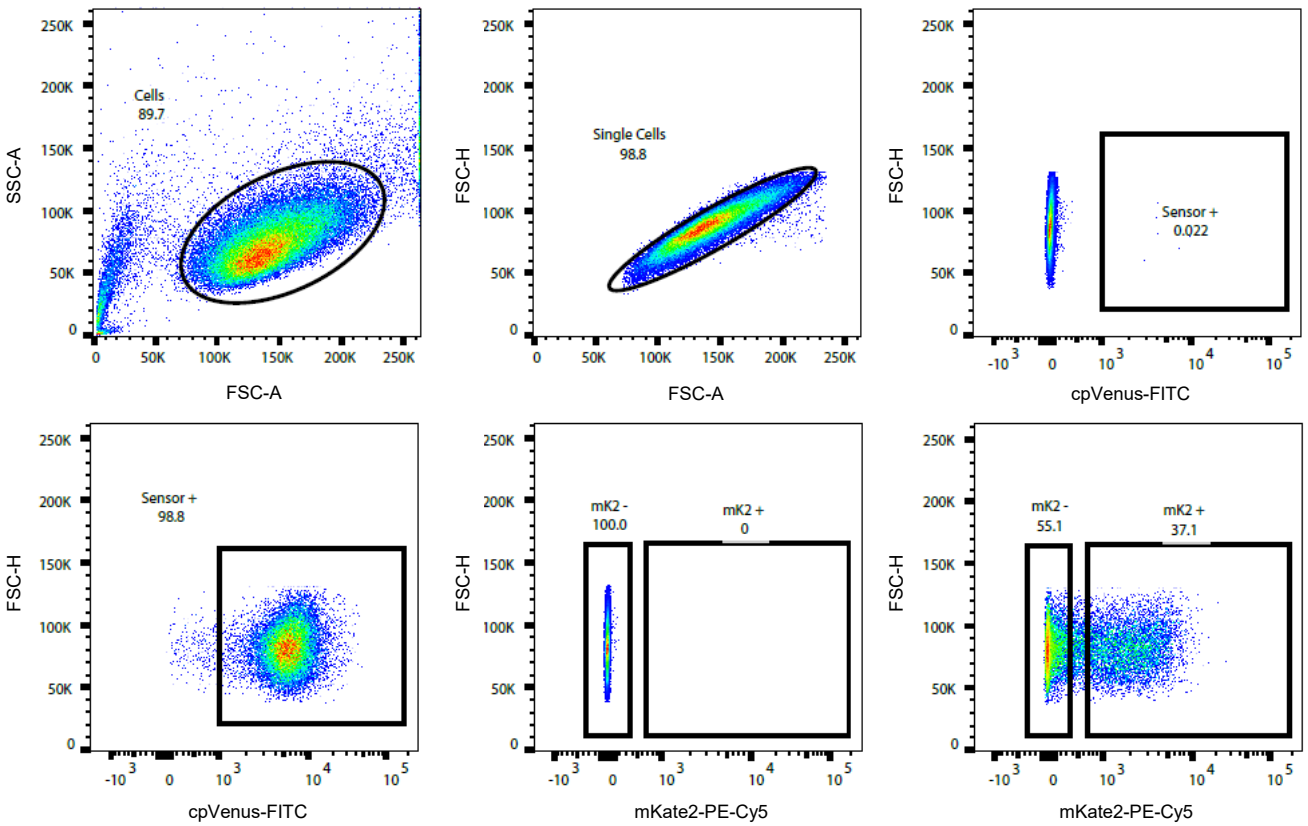

c

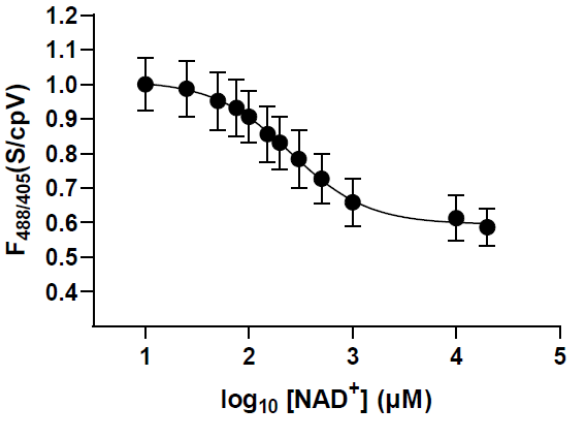

ED Figure 5

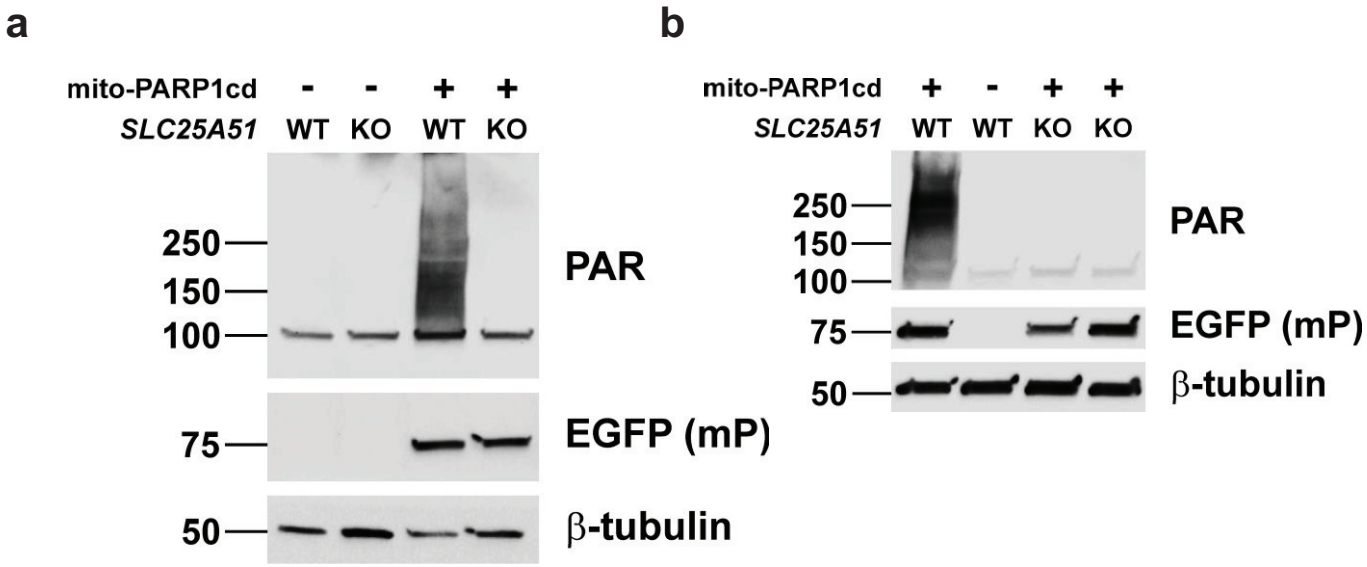
a
mito-PARP1cd - - + +
SLC25A51 WT KO WT KO
250
150
100
75
50
PAR
EGFP (mP)
β-tubulin
b
mito-PARP1cd + - + +
SLC25A51 WT WT KO KO
250
150
100
75
50
PAR
EGFP (mP)
β-tubulin

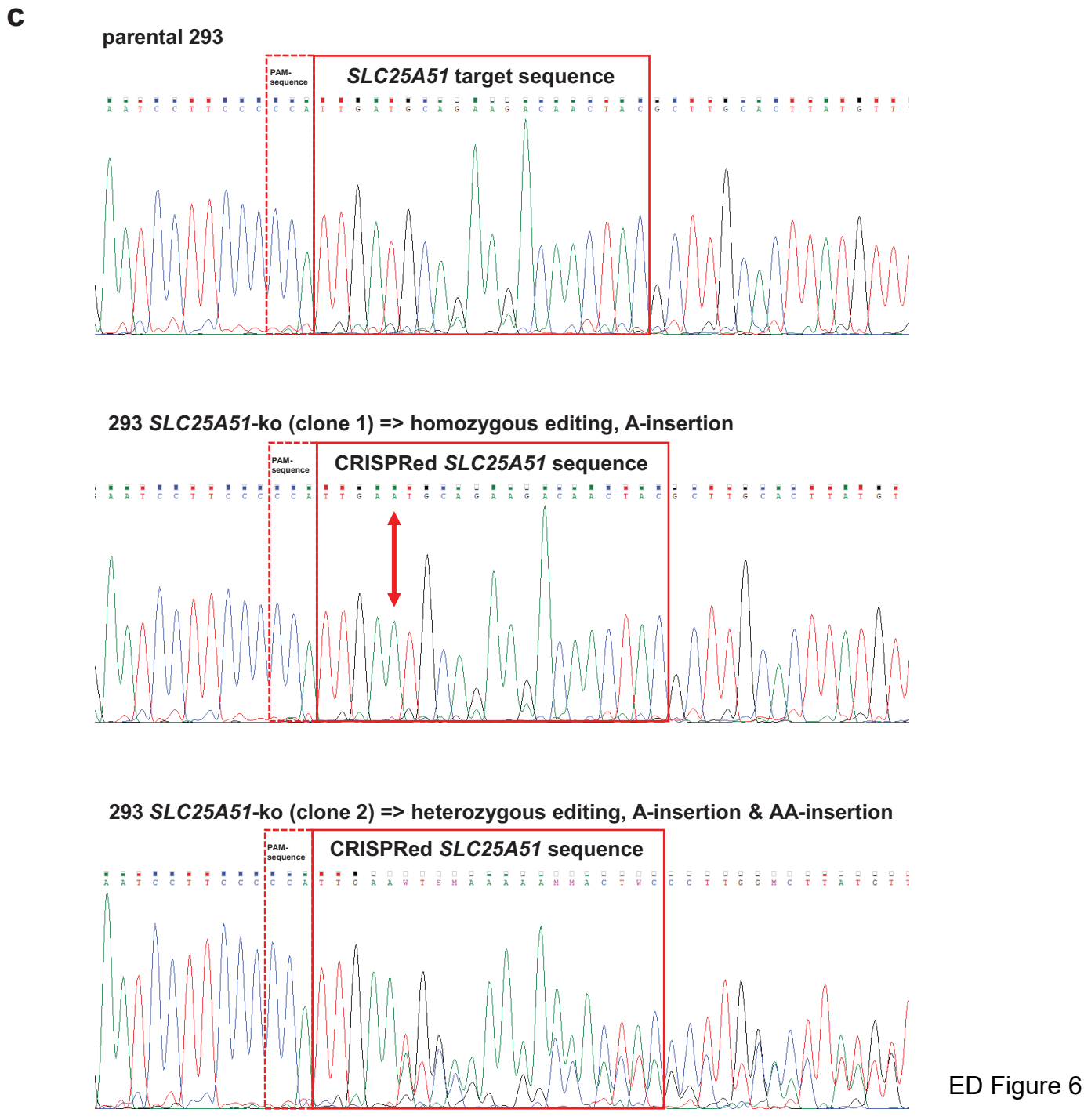
c
parental 293
PAM-sequence
SLC25A51 target sequence
293 SLC25A51-ko (clone 1) => homozygous editing, A-insertion
PAM-sequence
CRISPRed SLC25A51 sequence
293 SLC25A51-ko (clone 2) => heterozygous editing, A-insertion & AA-insertion
PAM-sequence
CRISPRed SLC25A51 sequence

ED Figure 6

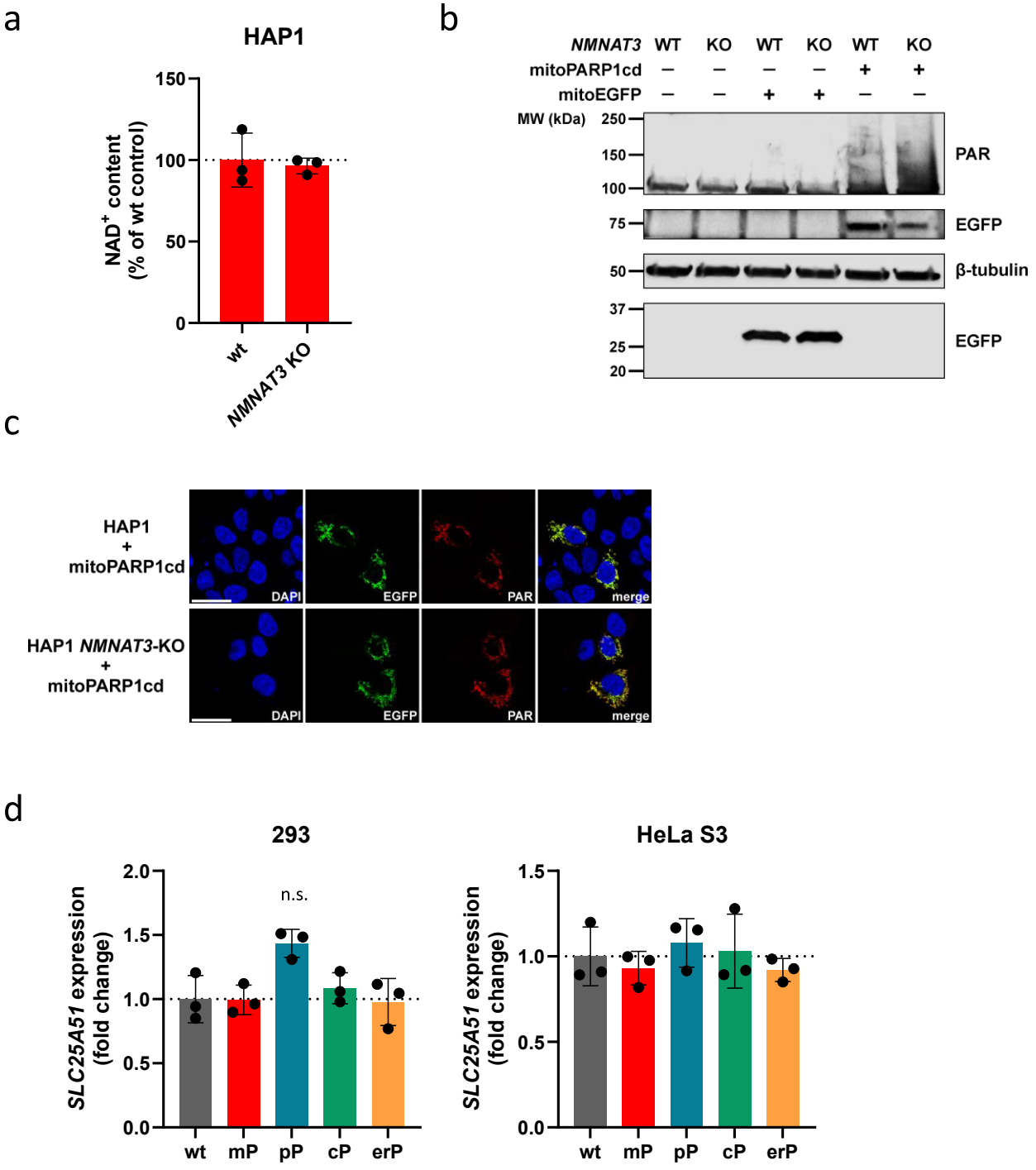
a
HAP1
NAD+ content (% of wt control)
150
100
50
0
wt
NMNAT3 KO
b
NMNAT3 WT KO WT KO WT KO
mitoPARP1cd – – – – + +
mitoEGFP – – + + – –
MW (kDa)
250
150
100
75
50
37
25
20
PAR
EGFP
β-tubulin
EGFP
c
HAP1 + mitoPARP1cd
HAP1 NMNAT3-KO + mitoPARP1cd
DAPI
EGFP
PAR
merge
d
293
HeLa S3
SLC25A51 expression (fold change)
n.s.
2.0
1.5
1.0
0.5
0.0
wt
mP
pP
cP
erP

ED Figure 7

parental 293

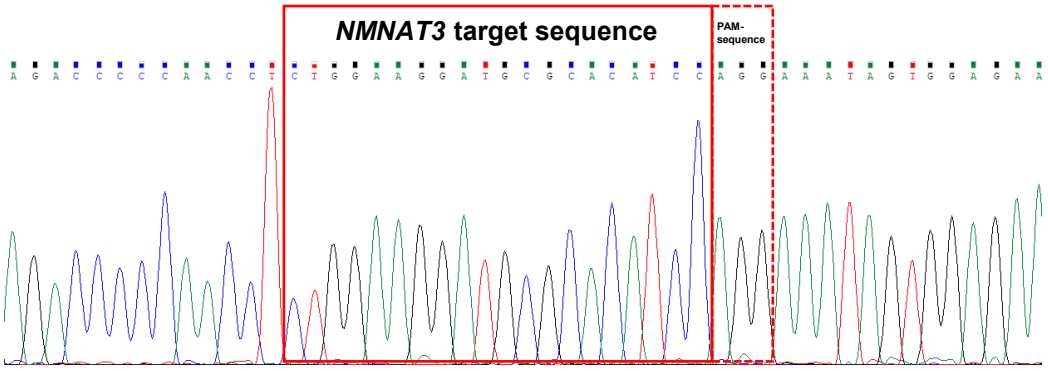

293 *NMNAT3*-ko (clone 1) => homozygous editing, A-insertion

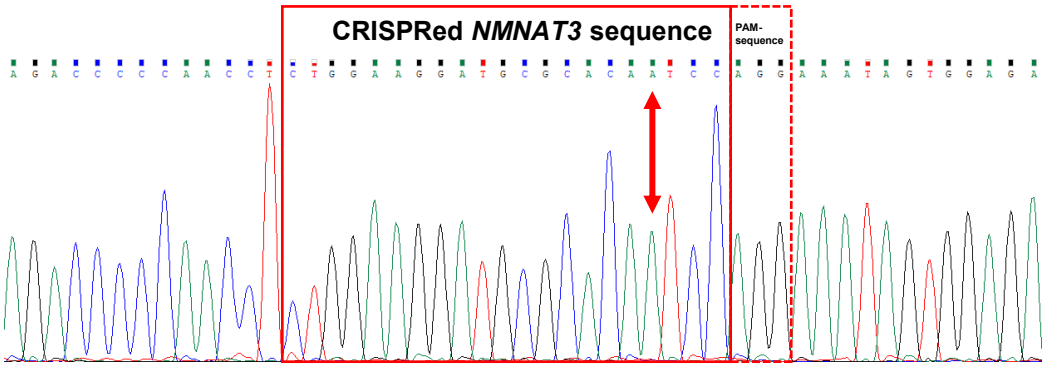

293 *NMNAT3*-ko (clone 2) => homozygous editing, 19 bp-deletion

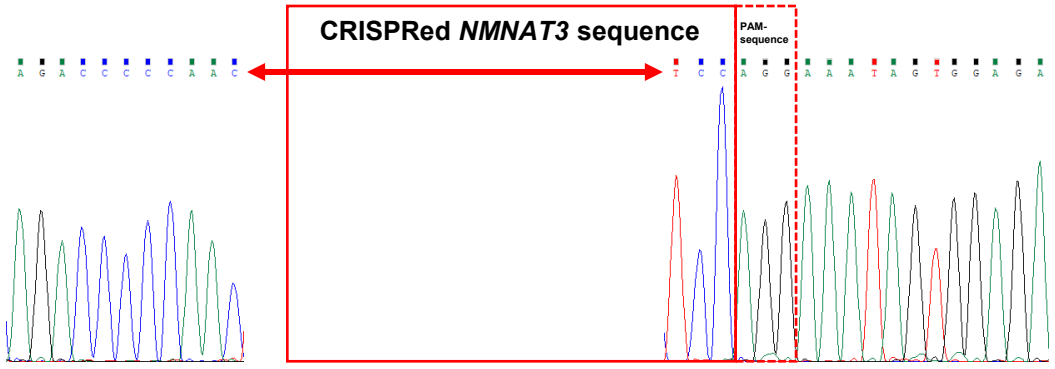

ED Figure 8

a

***NMNAT3*-ko in 293 mP => homozygous editing, A-insertion**

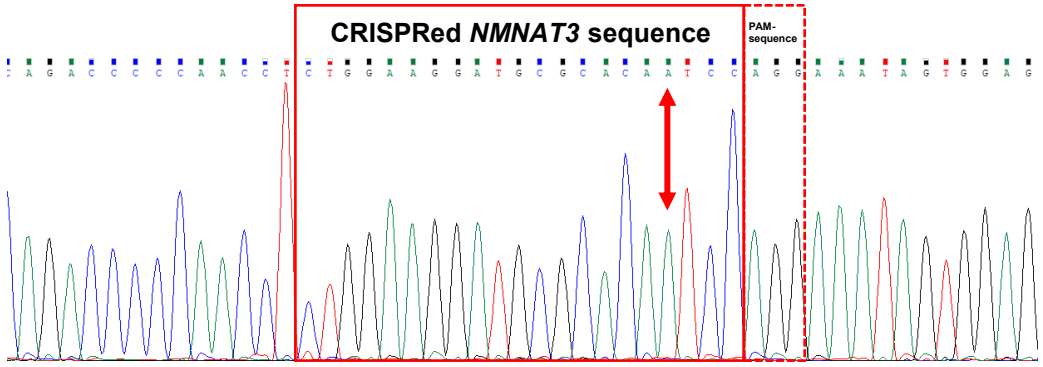

b

***SLC25A51*-ko in 293 NMNAT3-ko => heterozygous editing, A-insertion & AA-insertion**

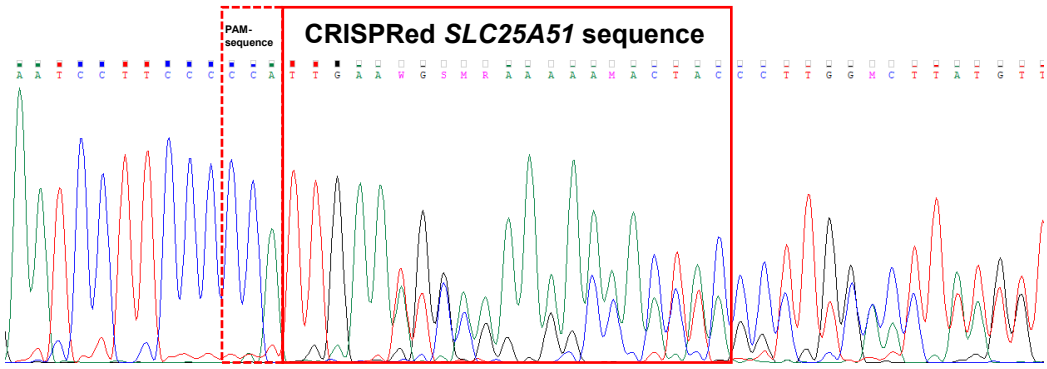

***Confirmation of NMNAT3*-ko in 293 NMNAT3/SLC25A51-dko)**

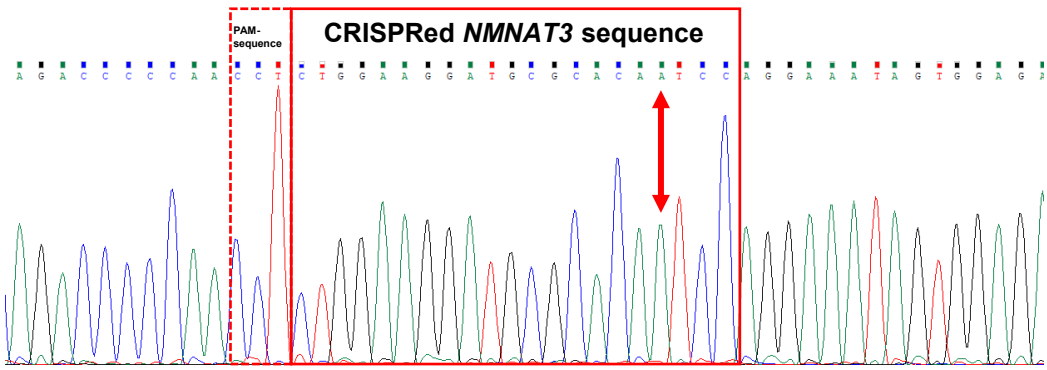

ED Figure 9